ORNL/SPR-2017/580

Radiation-Resistant Electrical Insulation Materials for Nuclear Reactors: Final Report

Robert Duckworth
Tolga Aytug
Parans Paranthaman
Georgios Polizos
Keith Leonard

March 2018

OAK RIDGE NATIONAL LABORATORY
MANAGED BY UT-BATTELLE FOR THE US DEPARTMENT OF ENERGY

ORNL/SPR-2017/580

RADIATION-RESISTANT ELECTRICAL INSULATION MATERIALS FOR NUCLEAR REACTORS: FINAL REPORT

Robert Duckworth
Tolga Aytug
Parans Paranthaman
Georgios Polyzos

Date Published: March 2018

Prepared for
US DEPARTMENT OF ENERGY
Office of Nuclear Energy
Nuclear Engineering Enabling Technology (NEET) Program

Prepared by
OAK RIDGE NATIONAL LABORATORY
Oak Ridge, TN 37831-6283
managed by
UT-BATTELLE, LLC
for the
US DEPARTMENT OF ENERGY
under contract DE-AC05-00OR22725

CONTENTS

LIST OF FIGURES

LIST OF TABLES

ABBREVIATIONS

ATR	attenuated total reflectance
DMA	dynamic mechanical analysis
DMAc	*N*-*N*-dimethylacetamide
EPR	ethylene propylene rubber
EPRI	Electric Power Research Institute
FTIR	Fourier transform infrared reflectometry
GIF	Gamma Irradiation Facility (at HFIR)
HDPE	high-density polyethylene
HFIR	High Flux Isotope Reactor
I&C	instrument and control
NPP	nuclear power plant
ORNL	Oak Ridge National Laboratory
PAA	poly(4,4′-carbonylbis(1,2-benzenedicarboxylic acid))-alt-(4,4′-methylenedianiline)
PE	polyethylene
PI	polyimide
PVA	polyvinyl alcohol
PVC	polyvinyl chloride
TBP	*tert*-butyl peroxide
TCB	1,2,4-trichlorobenzene
TEM	tunneling electron microscopy
TEOS	tetraethoxysilane
TGA	thermogravimetric analysis
(TMOSP)-DETA	(3-trimethoxysilylpropyl)diethylenetriamine
UV-Vis	ultraviolet–visible spectroscopy
VTES	vinyltriethoxysilane
XLPE	cross-linked polyethylene
XLPVA	cross-linked polyvinyl alcohol

ABSTRACT

The instrument and control cables in future nuclear reactors will be exposed to temperatures, dose rates, and accumulated doses exceeding those originally anticipated for the 40-year operational life of the nuclear power plant fleet. The use of nanocomposite dielectrics as insulating material for such cables has been considered a route to performance improvement. In this project, nanoparticles were developed and successfully included in three separate material systems [cross-linked polyvinyl alcohol (PVA/XLPVA), cross-linked polyethylene (PE/XLPE), and polyimide (PI)], and the chemical, electrical, and mechanical performance of each was analyzed as a function of environmental exposure and composition. Improvements were found in each material system; however, refinement of each processing pathway is needed, and the consequences of these refinements in the context of thermal, radiation, and moisture exposures should be evaluated before transferring knowledge to industry.

For PVA/XLPVA nanodielectrics, in situ methods were developed to allow for the uniform dispersion of SiO_2, TiO_2, and MgO. Within the dispersion, agglomeration was found only for XLPVA nanodielectrics with TiO_2, with particles on the order of 100 μm in diameter at 3 wt %. Improvements in dielectric breakdown strength and conductivity were observed for certain configurations of PVA/XLPVA nanodielectrics between 1 and 5 wt %, depending on the specific nanoparticle composition.

For PE/XLPE nanodielectrics, Fourier transform infrared spectroscopy (FTIR) indicated that SiO_2, Al_2O_3, and MgO bonded with the polymer chains of XLPE. The change in intensity of the Si–O–Si and Si–O–C bonds as measured by FTIR in the XLPE nanodielectrics was affected by oxidation that occurred during thermal (up to 120°C) and radiation (up to 18 MRad) exposures, and this oxidation depended on the weight percentage of the nanoparticles. Additionally, shifts in the permittivity of the XLPE nanodielectrics as a function of temperature, frequency, and weight percentage were also observed. These findings support the possibility of tailoring the weight percentage of the XLPE nanodielectrics to track aging and degradation via FTIR and frequency-based dielectric spectroscopy. Like PVA/XLPVA, improvement in dielectric breakdown strength was observed, with the degree of improvement depending on the specific nanoparticle composition. Further refinement of performance with respect to environmental exposures is needed to determine an optimal nanoparticle weight percentage.

For PI nanodielectrics, improvements in mechanical strength and dielectric breakdown strength were observed. While improvements were found from a limited number of thermal and radiation exposures, the relevance of the improvements in light of possible degradation due to moisture should be resolved in the context of the final baseline and accident conditions before PI nanodielectrics are considered.

1. BACKGROUND

The mechanical integrity and dielectric strength of cable insulations and jackets in nuclear power plant (NPP) instrument and control (I&C) cables provide plant operators with a reliable infrastructure for monitoring conditions and activating safety controls and auxiliary power systems during daily operations and off-normal emergency plant events. Compared with the conditions in other types of power plants, cable insulations and jackets in NPPs are exposed to elevated temperature, radiation, and humidity and must maintain their performance over a 40-year lifetime. While cable insulations such as cross-linked polyethylene (XLPE), ethylene propylene rubber (EPR), polyvinyl chloride (PVC), neoprene, and chlorosulfonated polyethylene have shown suitable radiation tolerance in laboratory tests [1,2] and met the requirements for cable insulations in current nuclear environments [3,4], a number of cable failures have been observed over a 30-year period under normal service conditions [3]. While investment in cable aging management programs by the NPPs in collaboration with the Long Term Operation Program at the Electrical Power Research Institute (EPRI) and improvements in cable manufacturing have reduced the risk associated with these issues [5], a gap in the performance of these insulations may not completely meet future and/or next-generation nuclear reactor requirements—that is, reactor operation for longer periods (60–80 years) under higher thermal and radiation transient and operating loads [6,7].

Nanocomposite dielectrics research has emerged with the desire to tailor dielectrics for specific applications. Conventional micron-sized additions to composite dielectric materials have long been used in the electrical insulation industry. Micron-size organic and inorganic fillers have been added to dielectric materials to improve properties such as mechanical strength and thermal conduction as well as to alter permittivity. However, the improvements in these physical properties come at a price: either the loss of electrical strength, high levels of partial discharge, or shortening of insulation life. As research has shifted toward the introduction of nanoparticles (10–100 nm), new physical properties have emerged. By reducing space charge and free volume, nanofillers have allowed the dielectric strength to remain high and reducing partial discharge. This in turn leads to longer insulation life under electrical stress. It is essential to note that the performance gains of nanocomposite dielectric materials are critically dependent on the uniform dispersion of particles and the elimination of particle aggregation. The in situ process developed by ORNL has demonstrated both nearly perfect dispersion (Fig. 1) *and* improved dielectric properties (Fig. 2) [8,9].

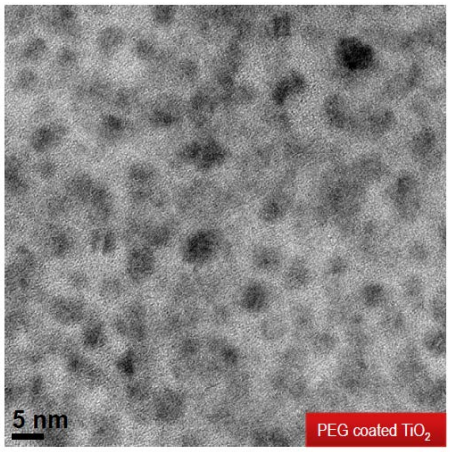

Fig. 1. Dispersion of polyethylene glycol (PEG) coated TiO_2 nanoparticles in polyurethane.

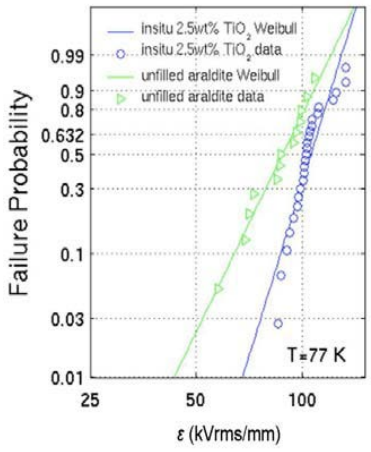

Fig. 2. Weibull plot showing improvement in breakdown strength for nanocomposite dielectric over base polymer [9].

Improvements in the dielectric properties of conventional dielectrics are connected to resistance to the phenomenon called partial discharge, where partial-discharge-induced damage occurs when an external field causes free electrons within the material to be accelerated to energies sufficient to break bonds and cause additional ionization. Partial discharge is an important mechanism for producing damage and ultimately leading to dielectric breakdown in polymers in high voltage applications. Given that high PD resistance generally correlates with high breakdown strength, comparison of the breakdown strength of materials with significant radiation resistance (Table 1) [10,11] indicates a possible connection (for polymers) between radiation and partial discharge resistance. With respect to improvements in these materials, it has been shown that the addition of nanometer sized fillers to XLPE, a commonly used insulation material in nuclear reactors, has exhibited two orders of magnitude improvement in insulation life (as measured by voltage endurance measurements shown in Fig. 3). Moreover, a recent report from Japan revealed that the addition of SiC nanoparticle filler at only 5 wt % led to a significant reduction in erosion rate over the base polymer when exposed for 480 h to partial discharge as shown in Fig. 4 [12].

Table 1. Radiation-tolerant polymers and corresponding breakdown strengths for 0.125 in. sample thickness

Polymer*	Breakdown strength (V/mil)	Maximum useful radiation dose (Gy)
PS	500	5×10^7
PI	560	2×10^7
PEEK	480	1×10^7
PC	380	6×10^5
Nylon	300–400	2.5×10^4

*PS, polystyrene; PI, polyimide; PEEK, polyether-ether ketone; PC, polycarbonate; Nylon, polyamide.

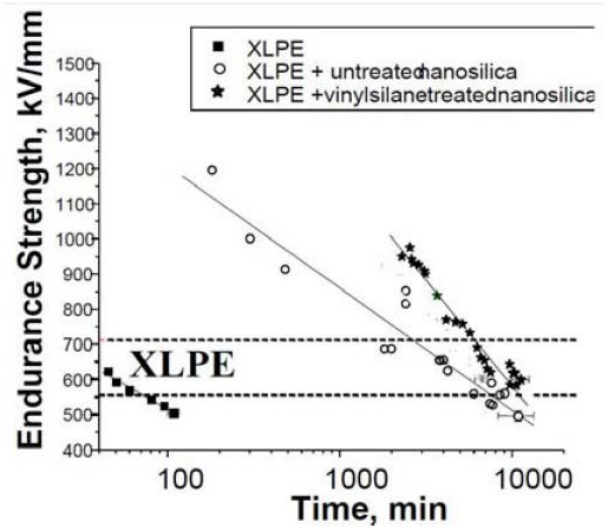

Fig. 3. Voltage endurance of XLPE and XLPE nanocomposites [10].

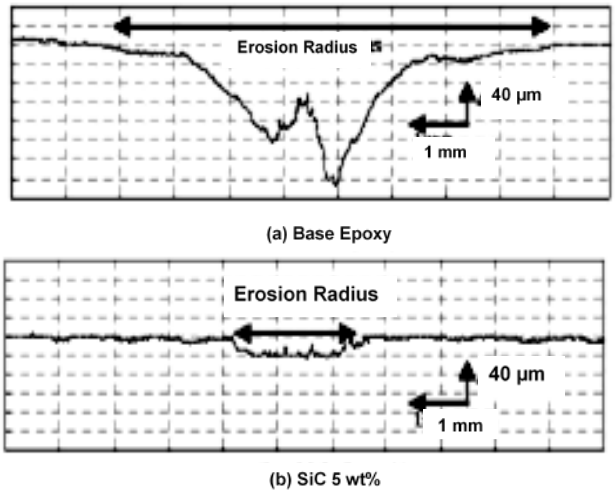

Fig. 4. Reduction in erosion rate when SiC nanoparticles are added at a relatively small weight percentage [12].

As one considers the improvements found in polymer dielectrics enabled by nanoparticles, the radiation degradation and/or tolerance of such materials relative to nuclear reactor environments should also be considered. In general, reactor irradiation environments consist of both gamma-ray (ionizing) and neutron (atomic displacement damage) components. For all reactor locations where polymer insulation is under consideration, radiation degradation is primarily through gamma radiation. Ionization and excitation in the electronic structure, known as electronic stopping, is the dominant process of gamma-ray interaction in materials. Though gamma rays can cause displacements in metals, energies greater than 2 MeV are required [13]. For polymeric materials, the ionization and excitation created by radiation can lead to radiolysis or the breaking of chemical bonds, leading to molecular scission or cross-linking and the related release of hydrogen or other low-molecular-weight gases. While resistance to thermal and chemical degradation in some polymeric materials is the result of fluorine–carbon or hydrogen–carbon bonds, which have the highest bond dissociation energies (530.5 and 429.7 kJ/mol, respectively), they are more sensitive to radiolysis than the weaker carbon–carbon (348 kJ/mol) bonds that typically comprise the molecular backbone [14–16]. The resulting excitations from irradiation are transferred along the main chain to the chain branches where it is localized [17]. Chain scission results in reduced molecular weights, reduced strength, and increased sensitivity to oxidation. While cross-linking increases molecular weights and increases strength, it also decreases ductility and compression properties. Increases or decreases in crystallinity can also occur in polymers irradiated under specific conditions depending on the starting structure of the material [18]. Furthermore, the primary mechanisms of chain scission and cross-linking can occur simultaneously in the same material, with one's domination over the other depending on parameters such as temperature [19], oxygen exposure [20], and type of radiation and dose rate [21].

Building upon this previous work, this project aimed to determine whether the improvements realized in nanodielectrics that were initially developed for cryogenic applications could translate into insulations for use in high radiation and temperature environments for advanced reactors. The technical approach was to develop three separate base resin systems into which nanoparticles could be incorporated either ex situ or in situ. Ex situ and in situ refer to the method of nanoparticle formation, where particles are either mixed into the base resin (ex situ) or formed within the resin through a chemical reaction (in situ). Samples with different nanodielectric compositions were exposed to systematic thermal and radiation exposure and their chemical, mechanical, and electrical properties were evaluated to track possible performance improvements. This report details the nanodielectric fabrication processes for each base resin system, gives their performance under different environmental exposures, and provides recommendations on their future development.

2. NANODIELECTRIC PROCESSING AND DEVELOPMENT

Over the course of this project, the goal was to develop practical material processing pathways that are consistent with current insulation fabrication methods so that improvements could be realized without adding significant processing costs. Three different base resin materials were selected on the basis of their feasibility for nanoparticle incorporation and final application: polyvinyl alcohol (PVA/XLPVA), polyethylene (PE/XLPE), and polyimide (PI).

2.1 PVA/XLPVA PROCESSING

The first base resin system investigated was PVA/XLPVA. The inclusion of in situ nanoparticles into PVA was based on guidance from several groups [22–25] that were developing PVA films for high-strength membranes and environmental coatings of solar cells and sensors. A process flow diagram for the PVA nanodielectrics is shown in Fig. 5. The in situ nanocomposite films were synthesized as follows. PVA (Sigma-Aldrich, 99% hydrolyzed form with an average molecular weight of ~70,000 amu) was dissolved in water at 95°C to prepare the matrix batch. The mixture appeared clear as the PVA dissolved. The amounts of both PVA and water were varied to control film thickness. The theoretical estimate of thickness was based on the density of PVA (1.26 g cm^{-3}), the area of the casting mold, and the amount of PVA in the total volume of mixture cast. The nanoparticle precursor solution was then added to the PVA along with 2 wt % *tert*-butyl peroxide (TBP) to initiate radical formation and cross-linking of the PVA chains when applicable, and the entire matrix was mixed for 1 h. The mixture was then cast onto the outer side of a 10 cm Petri dish covered with nonstick Teflon tape. The samples were then left at room temperature for ~48 h inside a laboratory hood. The film was carefully pulled off the Petri dish with plastic tweezers to minimize structural damage. The thickness of the films varied between 25 µm and 100 µm depending on the amount of the mixture.

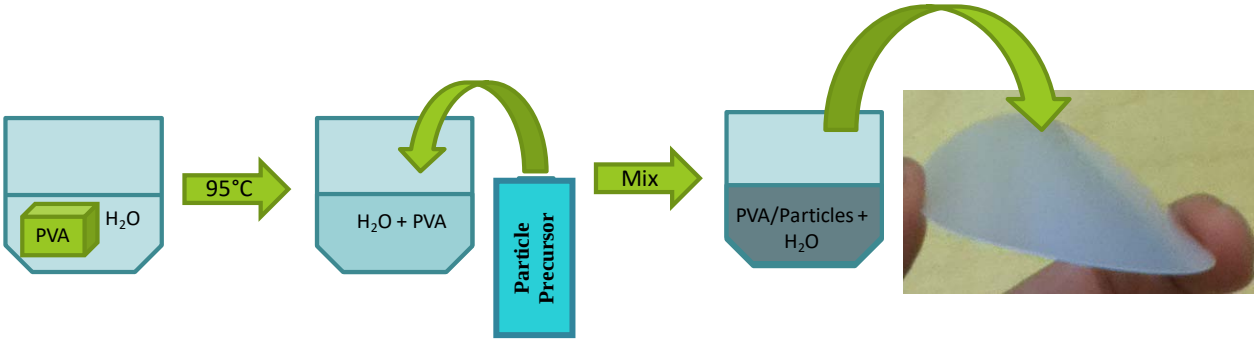

Fig. 5. Process flow diagram for formation of PVA/XLPVA films.

With respect to nanoparticle precursor solutions, three different compositions were investigated.

1. TiO_2 particle precursor solution was synthesized from a 1:10 volume ratio of titanium(III) chloride solution ($TiCl_3$ 20% in 3% hydrochloric acid) and water. The solution was then added to PVA at 95°C to produce mixtures with 0–15 wt % TiO_2 nanoparticles.
2. SiO_2 particle precursor solution was synthesized by dissolving silicic acid hydrate into tetrahydrofuran (THF) and stirring for ½ h. This solution was added to the PVA at 95°C along with 5.5 wt % vinyltriethoxysilane (VTES), which served as a surface modifier for the SiO_2 particles, to produce mixtures with 0–5 wt % SiO_2 nanoparticles.
3. MgO solution was synthesized by mixing $MgCl_2$ at a 20:1 to 30:1 ratio with deionized water. For large batches of precursors (>0.1 g $MgCl_2$), a septum-top vial and a heat-resistant glove were

needed to deal with the exothermic reaction. The solution was then mixed for 20–30 s in a vortex mixer and added to the PVA at 95°C.

2.2 PE/XLPE PROCESSING

Taking the processing lessons learned from the PVA/XLPVA process and recommendations from other groups [26–30], PE-based nanodielectrics were produced either by an in situ or ex situ process. While the focus on the project was to develop in situ processes to allow for integration into existing processes, the ex situ approach was pursued to allow for the properties of nanocomposite PE/XLPE films with different compositions to be studied without the time-consuming modification of the in situ process.

For the in situ PE/XLPE process, films started with high-density polyethylene (HDPE) in pellet form with an average molecular weight of 118,000. The SiO_2 precursor solution, which was prepared in similar fashion as the PVA/XLPVA films, was added along with 1,2,4-trichlorobenzene (TCB) to a Teflon beaker with HDPE, 4.8 wt % VTES, and 1.7 wt % TBP. Like the precursor solution, the VTES and TBP served functions similar to those in PVA/XLPVA processing, for surface modification of SiO_2 during formation and cross-linking of the polymer, respectively. TCB served to dissolve the HDPE. The beaker was then put in a hot oil bath and magnetically stirred until the bath temperature reached 125°C, at which point additional TCB equivalent to 20% of the original amount was added to the solution. Heating continued until the bath temperature reached 130–135°C, when the solution was removed from the heat and cast into a Teflon evaporating dish. This dish was then placed over a 135°C oil bath in the laboratory hood for 2–6 h to evaporate the solvent and then left in the hood overnight to cool.

In the ex situ process, fumed silica, along with desired amounts of HDPE, VTES, and TBP at the same weight percentages as were utilized in the in situ process, was fed into a DSM Xplore 5 cm^3 twin-screw Micro-Compounder and mixed at 200°C for 10 min before being extruded as filaments. The filaments were then placed between two 6 in. × 6 in. Teflon sheets. These sheets were sandwiched between two metal plates and placed in a Carver Auto Hot Press with the temperature set at 365°F (185°C), force set to 11,000 lb (48.9 kN), and dwell time set to 5 min. The Teflon sheets were removed from the press, allowed to cool for 30 min, and then pulled apart to remove the XLPE/SiO_2 films. The thickness of the films varied between 50 μm and 400 μm depending on the amount of the mixture. For MgO and Al_2O_3 nanodielectrics, powders of each with particle sizes averaging 50 nm were added at a given concentration at the same stage as the fumed silica to produce XLPE films with different concentrations of these additions.

2.3 PI PROCESSING

Polyimide/MgO/SiO_2/Al_2O_3 composite films with various MgO, SiO_2, and Al_2O_3 contents were prepared by a sol-gel process, shown in schematically in Fig. 6. Starting with poly(4,4′-carbonylbis(1,2-benzenedicarboxylic acid))-alt-(4,4′-methylenedianiline) (PAA, 18 wt %), (3-trimethoxysilylpropyl)diethylenetriamine ((TMOSP)-DETA) was added as a surface modifier to the PAA to ensure even dispersal of the nanoparticles from the MgO, Al_2O_3, or SiO_2 precursor solutions, which were added dropwise into the PAA solution,. The resulting mixture was stirred mechanically at room temperature for 5 h. The PI films were cast evenly on circular polytetrafluoroethylene (PTFE) plates between 2⅛ and 2¾ in. in diameter, dried at 70°C overnight, and annealed at 100°C for 1½ h and then at either 200°C or 300°C for 1 h. The thickness of the films varied between 50 μm and 200 μm depending on the amount of the mixture.

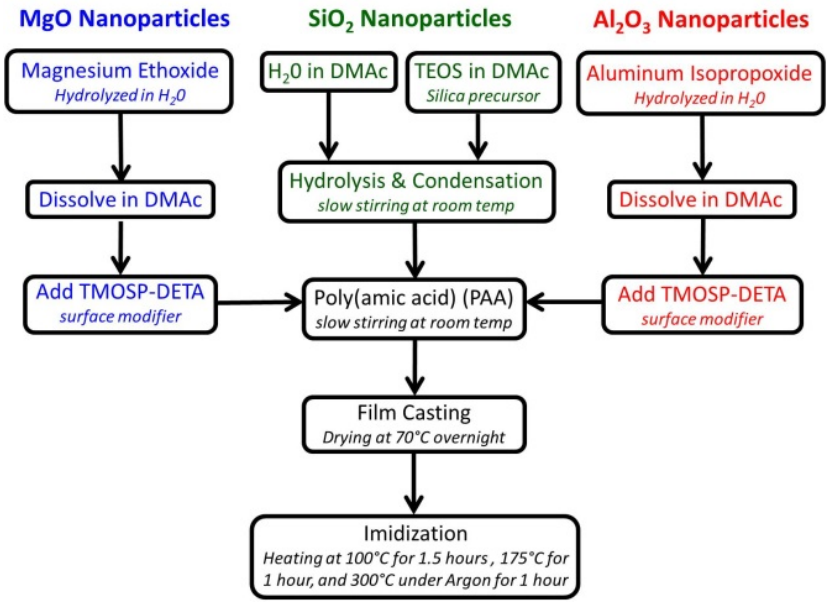

Fig. 6. Preparation of polyimide/SiO_2/MgO/Al_2O_3 samples.

The final heating at either 200°C or 300°C is related to the imidization process to fully convert PAA into PI. During the initial measurements of the mechanical and chemical properties of the PI nanodielectrics, it was found that this imidization temperature controlled the percentage of PAA that was converted into PI and ultimately its thermal stability as measured by thermogravimetric analysis (TGA). Figure 7 illustrates the TGA profile of the mass loss as a function of temperature for the two imidization temperatures, 200°C or 300°C. The mass loss represents the loss of water, oxidation, and/or volatile decomposition that occurs as the temperature increases. The TGA curve of the 200°C sample exhibited two steps of degradation, at 200–300°C and above 475°C. The sample annealed at 300°C had a less prominent first degradation that started at 250°C instead of 200°C. The improved thermal stability and the nanoparticle additions were two functional parameters examined to determine the impact of the imidization on PI nanodielectric performance.

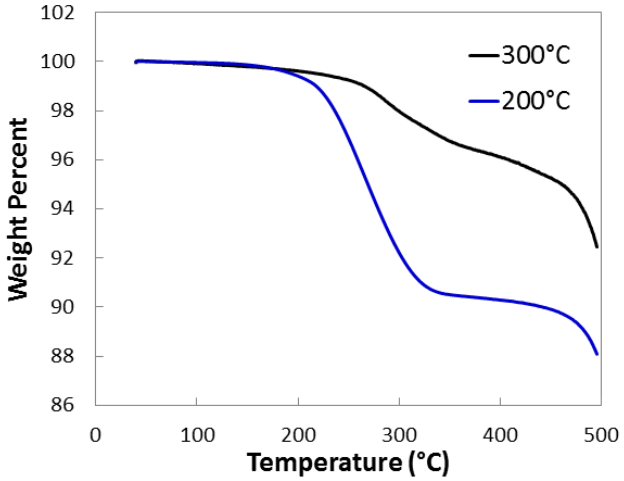

Fig. 7. Thermogravimetric analysis of polyimide base resin as a function of imidization temperature.

The precursor solutions for MgO, SiO_2, and Al_2O_3 were processed as follows.

1. SiO_2 particle precursor solution was synthesized by dissolving tetraethoxysilane (TEOS) and (TMOSP)-DETA into *N*-*N*-dimethylacetamide (DMAc, anhydrous, 99.8%). This mixture was then added to the PAA solution along with deionized water and DMAc to hydrolyze and condense the TEOS.
2. MgO or Al_2O_3 precursor solution was synthesized by hydrolyzing either the precursor magnesium ethoxide or aluminum isopropoxide in deionized water and then dissolving the solution in DMAc.

3. SAMPLE AGING AND PERFORMANCE CHARACTERIZATION

3.1 ACCELERATED THERMAL AND RADIATION AGING

To assess the impact of environmental exposure, performance of the nanodielectrics was examined through systematic exposures with respect to temperature and gamma irradiation. To examine the influence of temperature, accelerated aging of samples was carried out at temperatures between 80°C and 120°C in the air circulation furnace shown in Fig. 8. Figure 9 shows the appearance of XLPE nanodielectrics after exposure in air at 120°C for 5 weeks.

Fig. 8. Furnace used to perform accelerated thermal aging of nanodielectrics at temperatures between 100°C and 120°C.

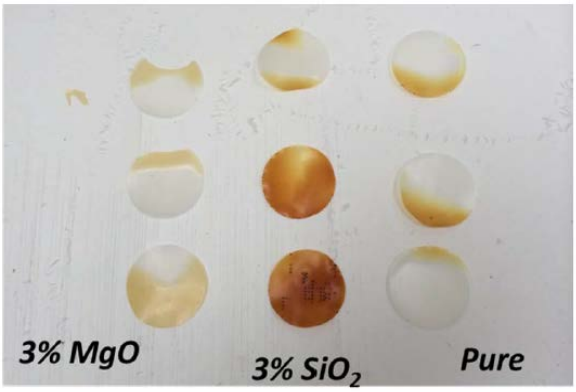

Fig. 9. XLPE nanodielectrics with different nanoparticle compositions after 5 weeks of exposure to air at 120°C.

Combined radiation and thermal exposure of nanodielectrics was carried at ORNL's High Flux Isotope Reactor Gamma Irradiation Facility (HFIR GIF). The GIF is in the HFIR reactor bay pool (Fig. 10) and consists of spent annular fuel assemblies from HFIR. The spent fuel provides a gamma source with dose rates ranging from 30 Gy/h to 100 Gy/h (0.03 Mrad/h to 10 Mrad/h) depending on the age of the fuel element and sample positions inside the canister (Fig. 11). Samples are placed in a specialized variable-position holder that is inserted into the canister and lowered into position within the flux trap of the spent fuel core. A variable gamma flux profile along the longitudinal direction of the flux trap of the spent fuel element is present and was utilized in this work to allow different accumulated dose levels to be tested within the same exposure run.

Fig. 10. Overhead view of spent fuel at the HFIR Gamma Irradiation Facility.

Fig. 11. Canister utilized for sample insertion into the HFIR GIF. Canister sample area has inner diameter of 8.0 cm (3.2 in.) and length of 60.9 cm (24 in.).

The sample holders and exposure configuration utilized for sample exposures in the HFIR GIF are shown in Fig. 12. Nanodielectric films were packed with 0.05-mm-thick aluminum foil spacers into packages that were inserted into the slots of the aluminum alloy sample holders. Aluminum alloy 6061 was selected as a compromise between maximizing thermal conductivity and minimizing gamma heating to maintain uniform sample temperature. For each sample holder, the springs that are shown in Fig. 12 allow for either low temperature (40–60°C) or high temperature (80–150°C). For low temperature exposures, the springs provide enough force to allow the side walls of sample holder to contact the canister side walls, which are at the pool temperature. When the springs are compressed for high temperature exposures, the sample holder temperature is influenced by the central heater element instead of the canister side wall. Two type K thermocouples, inserted into each sample holder, are connected to a heater control system to regulate the temperature to within ±2.5°C. The dose rate for a given sample holder is set by its position and the age of the spent fuel element surrounding the sample canister. The position of the sample holder takes advantage of the nonuniform radiation profile to allow for multiple dose rate exposures within a single run. The dose rate is measured through radiographic dosimetry films that were placed within each sample holder during each exposure.

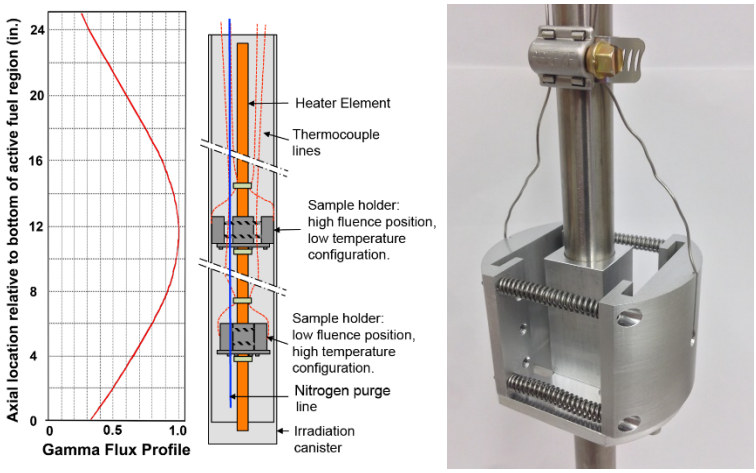

Fig. 12. *(Left)* longitudinal cross-section view of gamma profile in the HFIR GIF, along with a schematic of the sample fixture utilized, and *(right)* image of the sample holder without polymer films loaded into the vertical slots on each side of the holder.

While the HFIR GIF provided the best range of temperature and dose rates for sample exposures, an alternative option for radiation exposure was utilized during this project owing to delays from competing experiments at the HFIR GIF. The alternative option was a Co-60 irradiator (Fig. 13) that allows for a room temperature exposure with a dose rate of 140 Gy/h. Given the fixed temperature and dose rate, the Co-60 irradiator was used to perform radiation-only exposures with samples inserted into the canister to permit systematic removal of samples over a 28-d period (Fig. 14). Accelerated thermal aging was carried out on a portion of the irradiated nanodielectrics from the Co-60 source and compared to similar nanodielectrics that had only thermal aging to determine the differences between the two degradation mechanisms.

Fig. 13. Cobalt-60 irradiator utilized for nanodielectric sample exposures at room temperature and dose rate of 140 Gy/h.

Fig. 14. Irradiation sample holder with nanodielectric XLPE samples after 15-d irradiation at Co-60 source.

3.2 ELECTRICAL CHARACTERIZATION

Several different methods were used to quantify the electrical properties of the nanodielectrics with respect to composition and environmental degradation. When these properties are compared with chemical and mechanical properties, a better understanding of the polymer structure's influence and a possible optimal composition for a given base resin material are expected.

3.2.1 Dielectric Breakdown Strength

Dielectric breakdown strength was one method used to determine the performance limits of the nanodielectrics, as each had been successfully utilized to quantify performance improvements in previous studies [8–12]. For electrical breakdown strength, two approaches were taken. The first used a Phenix LD60 Oil Dielectric Test Set (Fig. 15) in conjunction with the test fixture (Fig. 16) to expose nanodielectric samples up to 60 kV at a ramp rate of 500 V/s. Samples were placed between the electrodes in Fig. 15 and the fixture was filled with Exxon Univolt insulating oil to increase the dielectric strength of the sample surroundings so that the electric stress was highest near the electrodes, reducing the likelihood of sample and electrode flashover. Multiple locations were tested by systematically moving the sample between the electrodes so that each breakdown occurred in a unique location. This was confirmed by observation of each test, the voltage breakdown, and post-test examination of each sample to check whether the number of breakdown locations matched the number of measurements. At least eight electrical breakdown strength measurements were conducted on a single sample in order to generate a statistically significant result for a given sample composition and environmental exposure.

Fig. 15. Phenix ac LD60 Dielectric Oil Test Set used for measurement of dielectric breakdown strength in nanodielectric films.

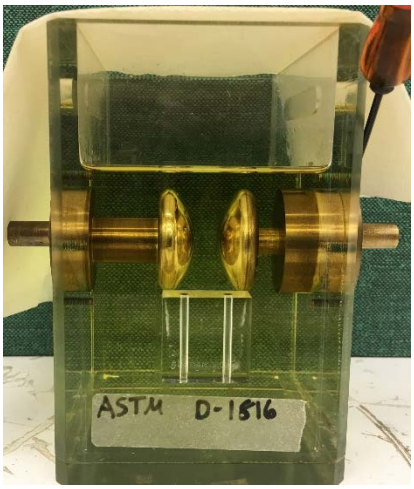

Fig. 16. Test fixture utilized with LD60 to measure dielectric breakdown strength in nanodielectric films. The fixture was filled with Exxon Univolt oil, and the film was placed between the pictured electrodes, which were moved until resting on the film surface.

The second method for dielectric breakdown strength, which was used when the sample diameter was greater than 5 cm, involved the deposition of silver electrodes (≈1 μm thick) with diameter of 5 mm on each side of the sample. The sample was then placed in a test fixture (Fig. 17) with high voltage probes attached to each silver electrode on the upper surface, and with a copper plate on the lower surface to reference all silver electrodes to ground. After the test fixture was lowered into an insulating container and immersed in Exxon Univolt insulating oil, the high voltage probe for a single location was connected to the 50 kV ac power supply (Fig. 18) and the voltage ramped at a rate of 500 V/s until a breakdown was observed. Post-measurement sample inspection was performed to ensure that breakdown did not bridge between locations. Like the other electrical breakdown strength, at least eight electrical breakdown measurements were carried out for a given sample. The two approaches were compared on base resin samples, confirming that the results from each approach were consistent with one another.

Fig. 17. Sample fixture illustrating silver electrodes deposited onto nanodielectric film and electrode placement for dielectric breakdown strength and voltage endurance measurements.

Fig. 18. Phenix 50 kV ac high voltage test setup that was connected to the sample fixture in Fig. 16 and utilized for measuring dielectric breakdown strength in nanodielectric films.

Given that dielectric breakdown strength is a measure of the statistical failure of a nanodielectric configuration, the dielectric breakdown strength was analyzed using a two-parameter Weibull distribution

analysis consistent with IEEE Standard 930-2004 [32]. A two-parameter Weibull distribution can be expressed by

$$F(E;\alpha,\beta) = 1 - exp\left\{-\left(\frac{E}{\alpha}\right)^{\beta}\right\} \quad (1)$$

where E is the measured variable (electric field – voltage divided by film thickness) and F(t) is the probability for failure at or below the measured variable. The scale parameter, α, is a measure of the nanodielectric performance at the electric field when the failure probability is 63.2% or $1 - 1/e$. The shape parameter, β, is a measure of the range of failure and is representative of the variation within the sample set. Small β would represent a consistent and/or reproducible failure mechanism, while large β could be the result of defects and/or nonuniformity within the samples under test. The application of the Weibull analysis to dielectric breakdown strength data is pictured in Fig. 19. The failure probability, F, is calculated from the expression

$$F(i,n) = \frac{i-0.44}{n+0.25} \quad (2)$$

where i is the test number and n is the total number of data points collected within the group. The scale and shape parameters, α and β, are calculated from the failure probability and measured variable data, and a regression analysis calculates the R^2 to measure the statistical accuracy of the parameters relative to the data obtained.

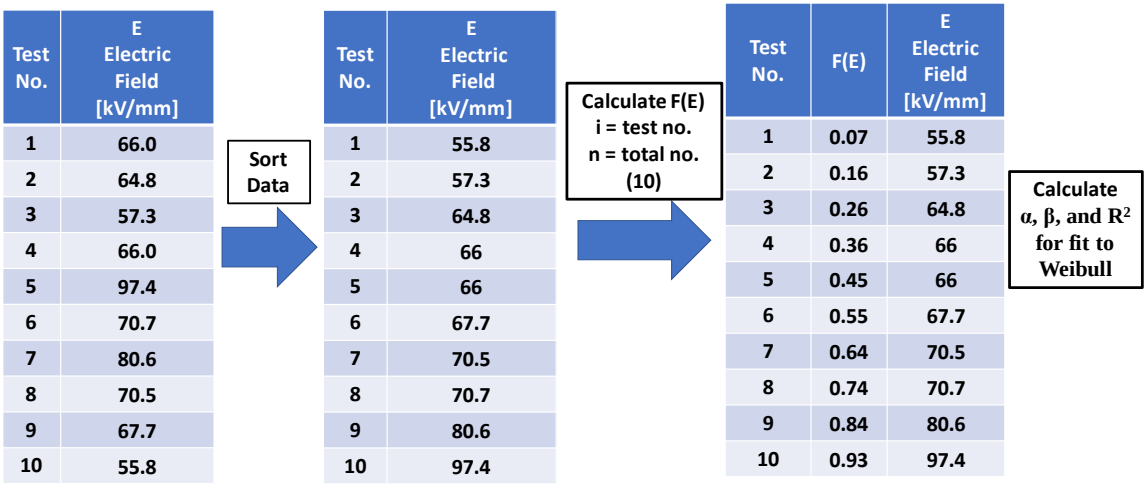

Fig. 19. Illustration of Weibull analysis utilized for dielectric breakdown strength.

3.2.2 Voltage Endurance

Voltage endurance measurements utilized the same test fixture and power supply as were used for the second electrical breakdown strength measurement. However, failure did not result from a voltage ramp but, rather, from a fixed voltage operated for an extended period at a voltage slightly below the electrical breakdown strength. The voltage output was measured with a phase-sensitive voltage divider, which tracks the partial discharge of the sample as a function of time. An example of the partial discharge observed in a nanodielectric prior to failure is given in Fig. 20. The voltage is then applied to another sample location at a different voltage to generate a voltage versus time profile similar to that shown in Fig. 3.

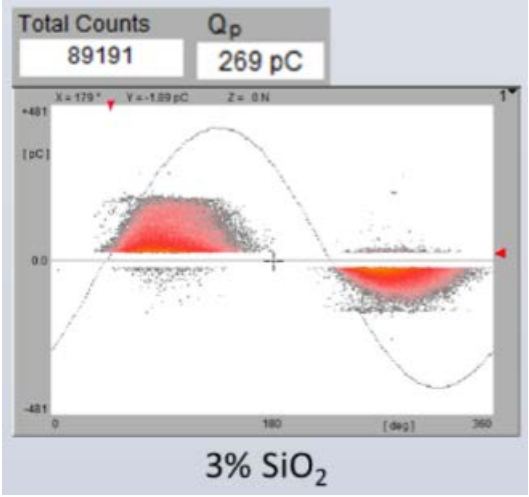

Fig. 20. Example of the partial discharge observed during voltage endurance measurement of XLPE nanodielectric with SiO_2.

3.2.3 Dielectric Relaxation Spectroscopy

In addition to electrical breakdown strength and voltage endurance, the dielectric properties of nanodielectric films were measured through dielectric relaxation spectroscopy. Samples were placed between two 20-mm-diameter electrodes and a Novocontrol Alpha-A impedance analyzer, and the complex permittivity was measured as a function of temperature from 0.1 Hz to 10 GHz. Examples of the real and imaginary permittivity as a function of temperature and frequency are given in Fig. 21.

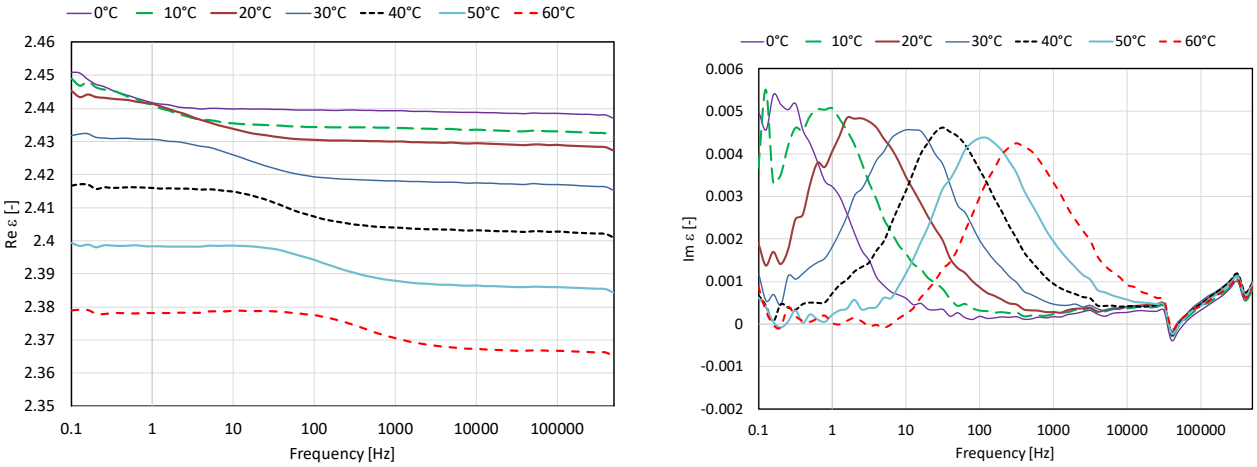

Fig. 21. Complex permittivity, real *(left)* and imaginary *(right)*, as a function of frequency and temperature for pure XLPE.

From the data in Fig. 21, the conductivity for a given nanodielectric film can be estimated, and when the temperature dependence is considered, an activation energy can be calculated as a property that represents the nature of the electrical structure of the insulation. If the real component of the impedance relates to an insulation resistance ΔR, the conductivity σ, which is the inverse of the resistivity, ρ, can be calculated with the expression $d/[A(\Delta R)]$, where d is the thickness of the sample and A is the surface area of the sample under measurement. Figure 22 shows the impact of TiO_2 on the permittivity of PVA as a function of temperature. Assuming that the temperature dependence of the conductivity follows an Arrhenius dependency of the form

$$\sigma(T) = \sigma_0 e^{(-E_a/k_B T)} \tag{3}$$

with σ_0 being a pre-exponential factor, E_a the activation energy, and k_B Boltzmann's constant, the activation energy can be found from a log–log plot of conductivity as a function of inverse temperature, as shown in Fig. 23.

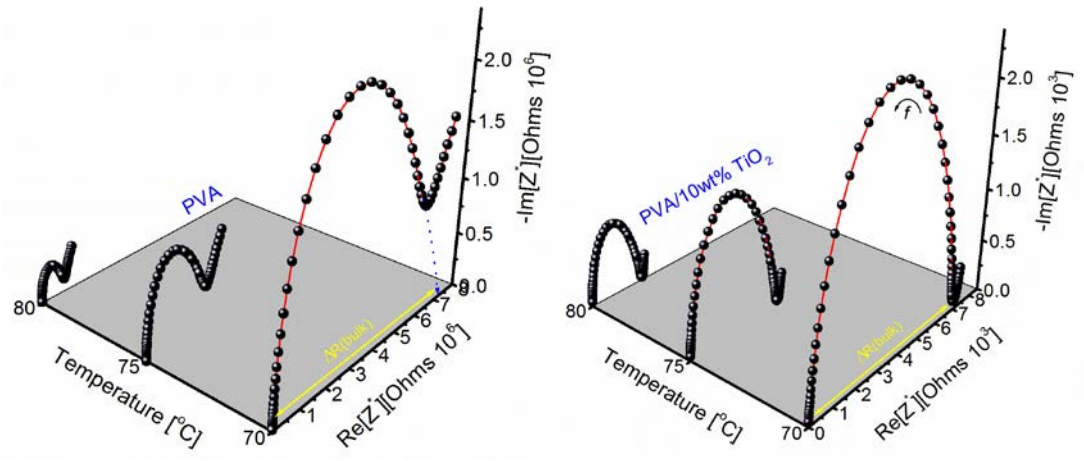

Fig. 22. Complex impedance plots illustrating the differences observed as a function of temperature for pure PVA *(left)* and PVA/10 wt % TiO_2 *(right)*. Note that the impedance of the pure PVA sample is three orders of magnitude higher than that of the PVA/TiO_2 composite system.

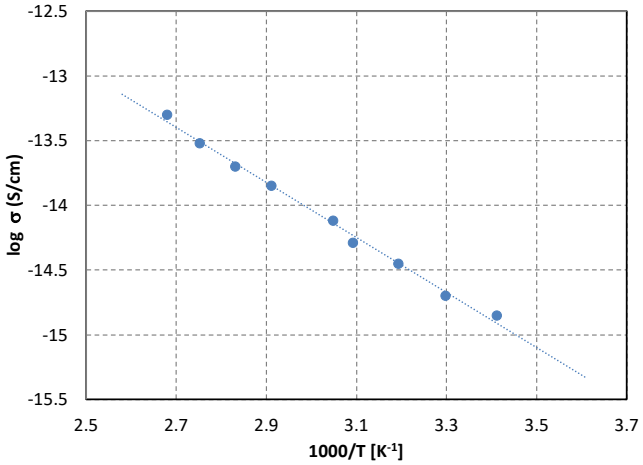

Fig. 23. Conductivity as a function of temperature (1000/T) for XLPE.

3.3 CHEMICAL CHARACTERIZATION

Chemical changes in the nanodielectrics for different nanoparticle compositions before and after environmental exposures were documented with either Fourier transform infrared reflectometry (FTIR), ultraviolet–visible spectroscopy (UV-Vis), or thermogravimetric analysis (TGA). FTIR utilizes infrared energy with respect to frequency to quantify the molecular vibration energy of a given material. The resultant interferometry pattern or spectrum generated is representative of the specific molecular bonds within the material, in our case the nanodielectric. Comparison of the different bonds with respect to the nanoparticles within a given base resin and their evolution with respect to environmental exposure should provide meaningful insights on the impact of nanoparticles and their bonds on electrical and mechanical properties of the nanodielectric. Over the course of the project, FTIR spectra were collected by use of a

Digilab Fourier transform spectrometer (FTS) 7000 equipped with a deuterated triglycine sulfate (DTGS) detector and a PIKE MIRacle attenuated total reflectance (ATR) accessory with a diamond crystal. Sixty-four scans were taken at a resolution of 4 cm^{-1}, and multiple locations for a nanodielectric were sampled to evaluate its homogeneity.

UV–Vis spectrometry was employed to characterize the dispersion and size distribution of nanoparticles in the nanodielectrics. The transmitted intensity through a given polymer is affected by the angle of incidence, its wavelength, the refractive index of the material, and the size of the particles within the material. Through variation of the wavelength of the incident source and comparison of the UV spectra of the pure base resin, the measured intensity can reveal the average size of particles and any possible changes to the covalent bond structure of the material. UV–Vis spectra were obtained on a Shimadzu UV-1800 spectrometer. The transmittance of the films was sampled over the measurement wavelength range, from 1100 to 190 nm, at a scanning rate of 0.5 s and intervals of 2 nm.

3.4 MECHANICAL CHARACTERIZATION

In addition to chemical and electrical properties, mechanical properties of the polymer films were measured to further track the impact of nanoparticles in unaged and aged nanodielectrics. When sufficiently thick films (>250 μm) were produced, 0.5 cm wide by 2.54 cm long strips were cut and inserted into an Instron Model 5560 tensile tester. A load was applied and the stress as a function of displacement was recorded until failure was achieved.

For thin samples, the mechanical properties of the nanodielectric were obtained through dynamic mechanical analysis (DMA) performed on a TA Instruments Rheometrics solids analyzer, RSA III, using rectangular tension/compression geometry and a frequency/temperature sweep test. A strain of 0.05% was applied while sweeping at 0.1, 1, 10, and 99 Hz and from 30°C to 400°C in increments of 2°C in an air atmosphere. The average dimensions of the films tested were 15–20 mm in length, 10 mm in width, and 150 μm in thickness. They were longitudinally deformed by a sinusoidal stress, and the resulting strain was measured. The storage modulus E', loss modulus E'', and loss tangent ($\tan\delta = E''/E'$) were recorded. The activation energy E_a was extracted from the slope of the linear fit when the natural log of the frequencies ($\ln f$) versus the glass transition temperature (T_g) of the polymers was plotted.

4. RESULTS AND ANALYSIS

4.1 PVA/XLPVA

The interaction of the nanoparticles with respect to the PVA/XLPVA base resin was examined by use of tunneling electron microscopy (TEM), UV-Vis, and FTIR. Uniform dispersion of nanoparticles within the PVA/XLPVA base resin for TiO_2 and SiO_2 was observed from TEM images (Figs. 24 and 25). However, at lower resolutions the PVA/TiO_2 films clearly had larger nanoparticles and a tendency for agglomeration. This agglomeration was further supported by UV-Vis spectrometry for the PVA/TiO_2 (Fig. 26) and PVA/SiO_2 (Fig. 27) as a concentration dependence in the transition near 300 nm was observed in the PVA/TiO_2. The lack of a shift in the UV-Vis spectra of PVA/SiO_2 supports uniform dispersion for particles less than 200 nm.

With respect to the chemical bonds between the PVA and the nanoparticle additions TiO_2 and SiO_2 and their impact due to concentration, FTIR spectra in Figs. 28 and 29 indicate that the TiO_2 had an appreciable interaction with the PVA while the SiO_2 showed little response. Titania particles form by linking titanium and oxygen, and they interact with PVA mainly by forming C–O–Ti bonds. Ti–O or Ti–O–Ti peaks may be visible in the 700–1000 cm^{-1} range. Due to the high overlapping of peaks in that region, it is difficult to

distinguish between the Ti–O and Ti–O–Ti bonds. A C–C stretching vibration peak is also visible at approximately 1100 cm^{-1}. The broadening –OH peak around 3300 cm^{-1} suggests that fewer –OH groups are interacting with PVA through hydrogen bonding. These observations were consistent with those observations of PVA with TiO_2 nanoparticles [31]. A broad band of between 3600 cm^{-1} and 3000 cm^{-1}, corresponding to the O-H vibration mode was observed in the spectra. In the PVA spectrum, a band at ca. 863 cm^{-1}, attributed to the C-C stretching mode and C-H rocking of PVA, decreased while redshift in the TiO_2 PVA spectra indicated interaction between TiO_2 nanoparticles and the PVA chains. In the range of 1000–1600 cm^{-1} observed bands at ca. 1100, 1320 and 1430 cm^{-1} corresponding, respectively, to the stretching vibration mode of the C-O and bending CO-H and H-C-H, in the PVA molecule. The bending vibration mode of the C-OH bond (1635 cm^{-1}) also shifts. The decrease and-shift of bands at 1089 and 1320 cm^{-1} in the spectra of nano-composite (TiO_2- PVA) confirmed interaction of the TiO_2 nanoparticles with PVA. Based on these results, the possibility of a mechanism for organic surface modification of TiO_2 nanoparticles was confirmed. Unlike the PVA/TiO_2, little change in FTIR spectra was observed in the filled and unfilled PVA/SiO_2 samples. When combined with the TEM and UV-Vis, these results suggest that the silane added to produce SiO_2 formed particles in situ but that the covalent nature of SiO_2 prevented its interaction with the PVA base resin.

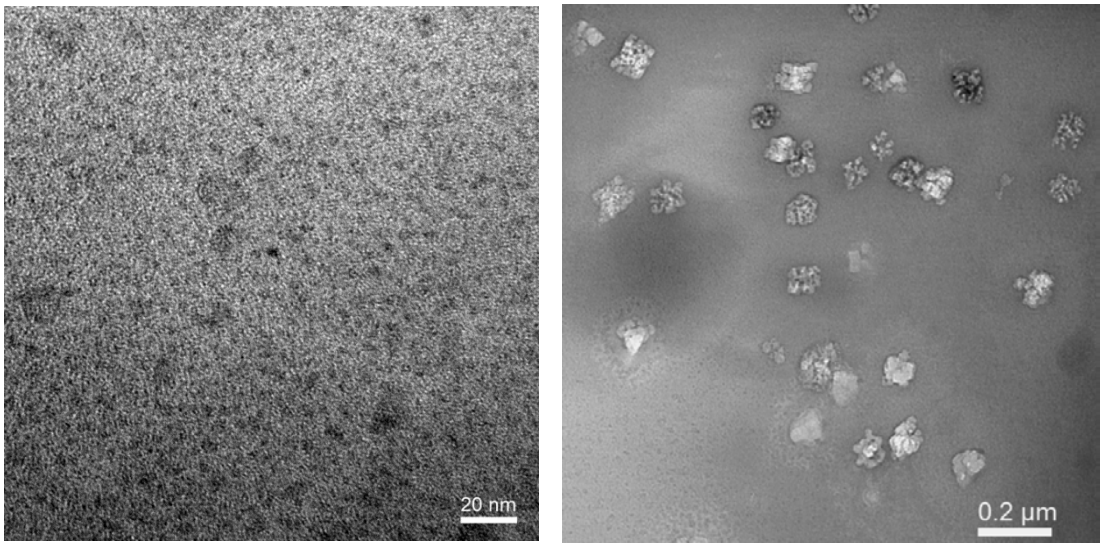

Fig. 24. TEM images of PVA/TiO_2 (3 wt %) nanodielectric at two length scales.

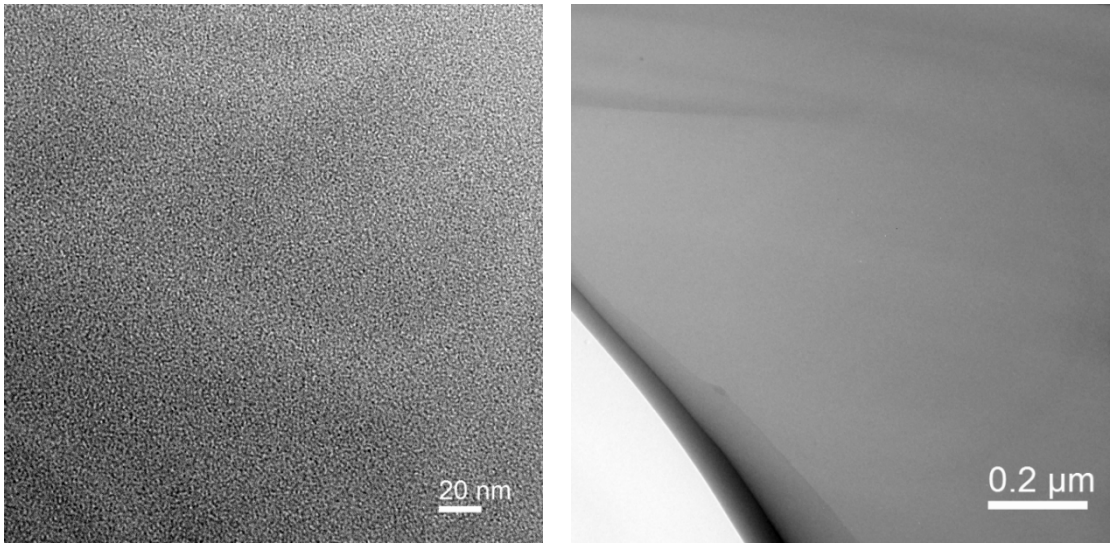

Fig. 25. TEM images of PVA/SiO_2 (3 wt %) nanodielectric at two length scales.

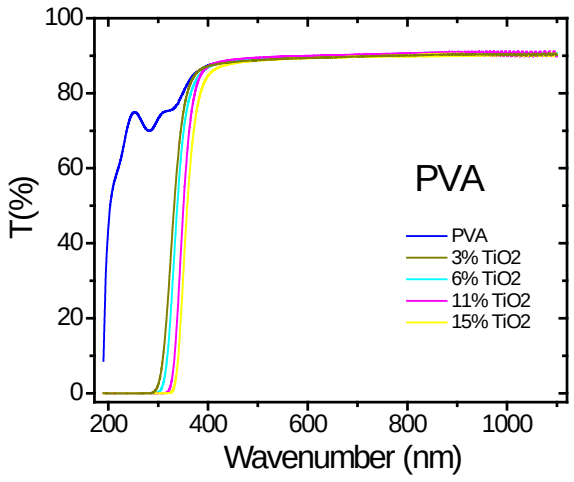

Fig. 26. UV-Vis spectrum with respect to transmittance (T%) for PVA nanodielectric films with different concentrations of TiO_2.

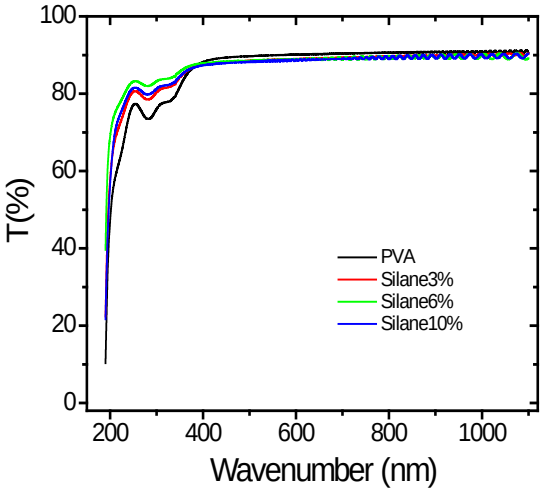

Fig. 27. UV-Vis spectrum with respect to transmittance (T%) for PVA nanodielectric films with different concentrations of SiO_2 (silane).

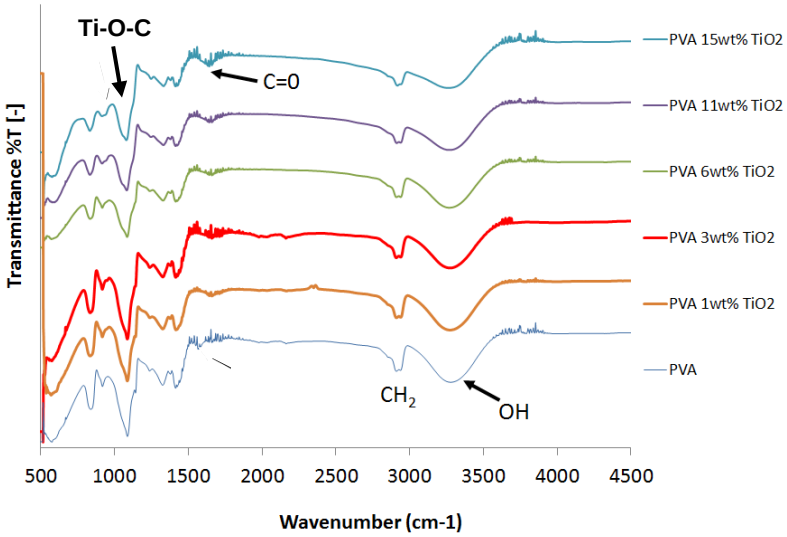

Fig. 28. FTIR spectra of PVA nanodielectric films with different concentrations of TiO_2.

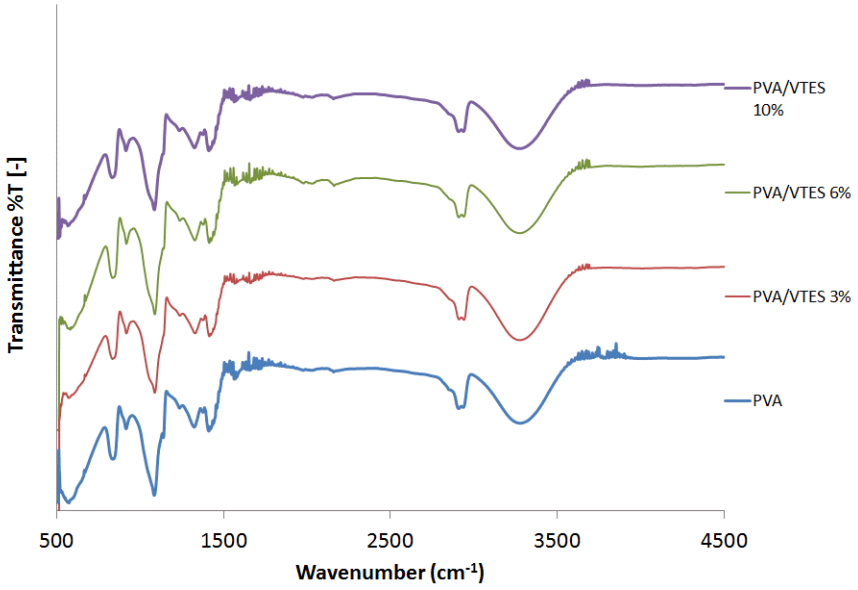

Fig. 29. FTIR spectra of PVA nanodielectric films with different concentrations of SiO_2 (VTES).

With respect to electrical properties, Figs. 30 and 31 show the impact of the type of nanoparticle addition and its concentration on electrical conductivity. For TiO_2, no appreciable change in conductivity is observed until the percentage reaches above 10 wt %. This increase in conductivity results in a drop of resistance by two to three orders of magnitude. This could be supported by the growth of TiO_2 agglomeration at the increased weight percentage and resultant titanium interconnections, although further modeling is needed to confirm. For SiO_2, conductivity data does not demonstrate a functional increase with increasing weight percentage. Note that the films in Fig. 31 were made with XLPVA, not PVA. The application of XLPVA was driven by the desire to improve bonding between SiO_2 and the base resin and to improve the high temperature performance of PVA. XLPVA with TiO_2 was not produced due to its precursor's inability to retain TiO_2 at the higher cross-linking processing temperature. Unfortunately, UV-Vis and FTIR were not collected to confirm the performance of SiO_2 relative to XLPVA since the PVA was an initial model system and its high temperature range was low (80–100°C) when compared to XLPE and PI. Improvement in

dielectric breakdown strength was observed in XLPVA when SiO_2 and MgO precursor solutions were added (Figs. 32 and Figs. 33). The observed drop in dielectric breakdown strength as the percentage of nanoparticles increased is likely the result of increased agglomeration and defects; however, further examination is required. While the limited exposure of XLPVA and PVA films to gamma irradiation showed mixed results, the use of XLPVA and PVA films in low temperature, high radiation environments would require additional development, but the processing pathway for cross-linking PVA is new and could have other tangible benefits.

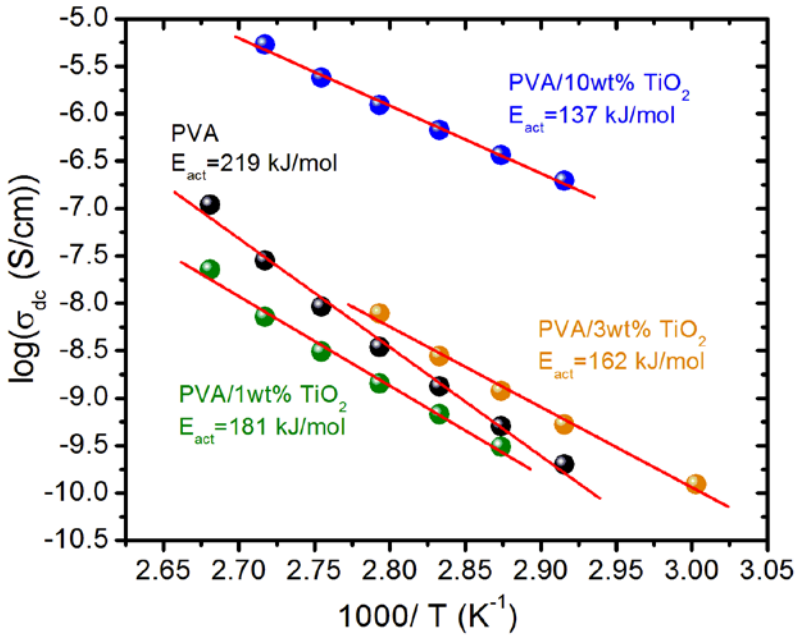

Fig. 30. Estimated conductivity of PVA with respect to temperature (1/T) and weight percentage of TiO_2.

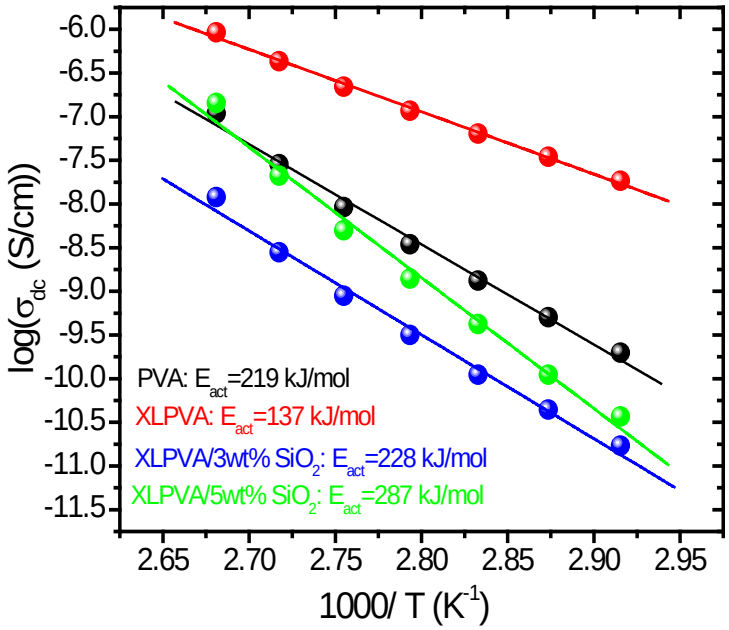

Fig. 31. Estimated conductivity of PVA and XLPVA with respect to temperature (1/T) and weight percentage of SiO_2.

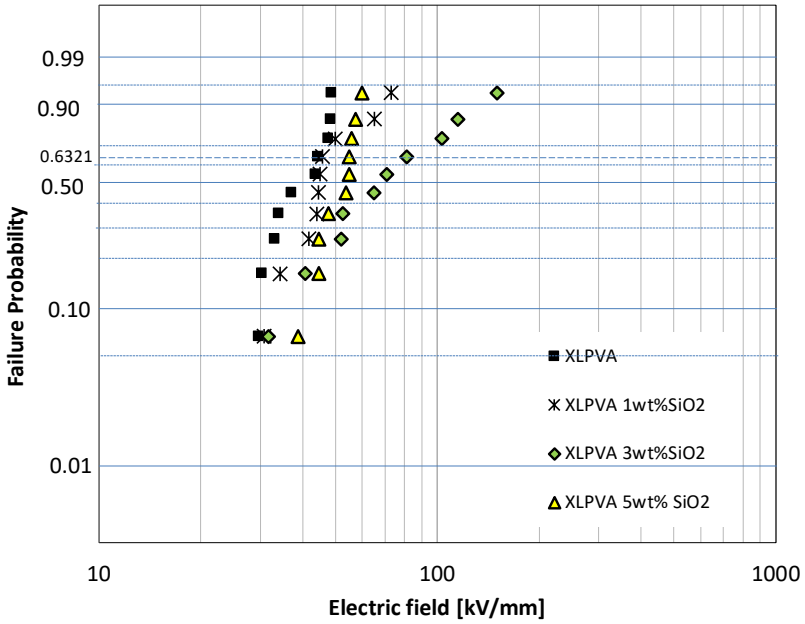

Fig. 32. Weibull distribution of the dielectric breakdown strength of XLPVA as a function of SiO_2 weight percentage.

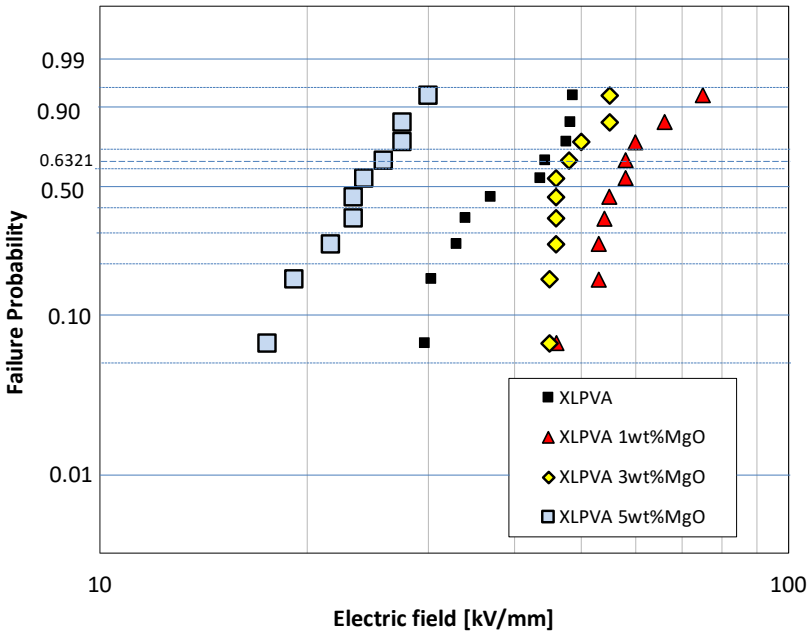

Fig. 33. Weibull distribution of the dielectric breakdown strength of XLPVA as a function of MgO weight percentage.

4.2 PE/XLPE

Of the three base resin materials, more than 50% of the nanodielectrics generated and measurements taken were on PE and XLPE nanodielectrics. This was driven by the applicability of XLPE in current cables for high temperature, high radiation, and high moisture applications. UV-Vis spectra were utilized to examine the dispersion of nanoparticles in XLPE, with examples shown in Figs. 34 and 35 for SiO_2 and MgO respectively. Unlike PVA-based nanodielectrics, the increase in the weight percentage of the nanoparticles

had a significant impact on the UV spectra, with the transmission percentage dropping significantly as the wave number increased. This suggests that agglomeration was more prevalent in this material system.

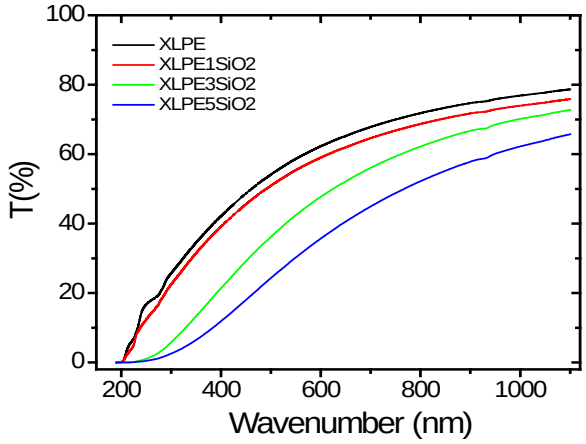

Fig. 34. UV-Vis spectra with respect to transmittance (T%) for XLPE nanodielectric films with different concentrations of SiO_2.

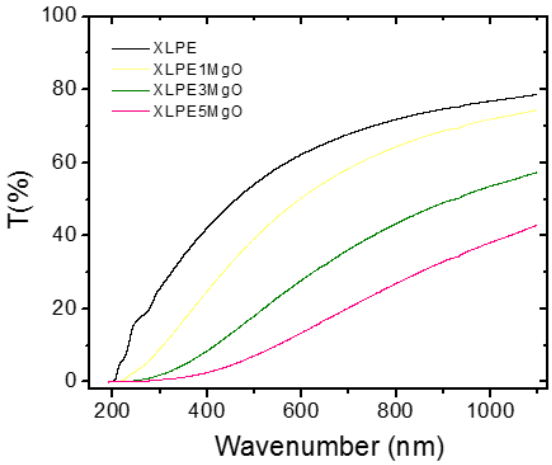

Fig. 35. UV-Vis spectra with respect to transmittance (T%) for XLPE nanodielectric films with different concentrations of MgO.

While TEM images were unable to confirm agglomeration like that in the PVA nanodielectrics, FTIR measurements of the films before and after environmental exposures confirmed that the nanoparticle additions did interact with the chemical structure of the XLPE. Prior to environmental exposures, changes in transmittance as a function of SiO_2 were observed; specific changes near 1140 cm^{-1} and 820 cm^{-1} (Fig. 36) were attributed to vibrational modes associated with Si–O–Si bonds. When accelerated thermal aging was carried out at 120°C on XLPE nanodielectrics with a fixed 3 wt % SiO_2, new peaks at 1715 cm^{-1} and 1728 cm^{-1} formed (Fig. 37) from the oxidation of polyethylene, while the shift in the Si–O–Si peak toward 1168 cm^{-1} indicated the formation of Si–O–C and/or Si–C_2H_5 bonds as oxygen interacted with the Si in the film. When films were exposed to gamma irradiation at the HFIR GIF up to an accumulated dose of 18 Mrad in an inert environment, no change in the FTIR spectra was observed (Fig. 38) except that associated with the Si–O–Si bonds mentioned earlier. From a series of sequential radiation exposures in air at the Co-60 source up to 10 MRad followed by a 21-d accelerated thermal aging at 120°C, the change in FTIR spectra observed in Figs. 39 and 40 was again attributed to oxidation. This oxidation was driven by both the radiation and thermal aging as a measurable response near 1715 cm^{-1} and 1728 cm^{-1}. The dependence of magnitude of these peaks appeared to correlate to the accumulated dose and thermal aging, with the peak height greatest for 10 MRad with thermal aging. When the nanoparticle was changed to MgO, changes in the FTIR spectra for the same environmental exposure were observed. Peak at 1710 cm^{-1} for both cases in Fig. 37 would be consistent with oxidation observed earlier, but lack of change in the peak magnitude might suggest that the MgO cut down this oxidation. However, changes near 3400 cm^{-1} and 1630 cm^{-1} (-OH stretch and bending of C-OH) and 1480 cm^{-1} (C-H bend) suggest that oxidation is inducing the formation of magnesium ethoxide like species. Further systematic study of this formation is needed to confirm these observations and their significance toward nanodielectric performance. Overall, FTIR spectra of XLPE nanodielectrics provided a meaningful understanding on the systematic change and the impact of environmental degradation on the chemical structure of nanodielectric.

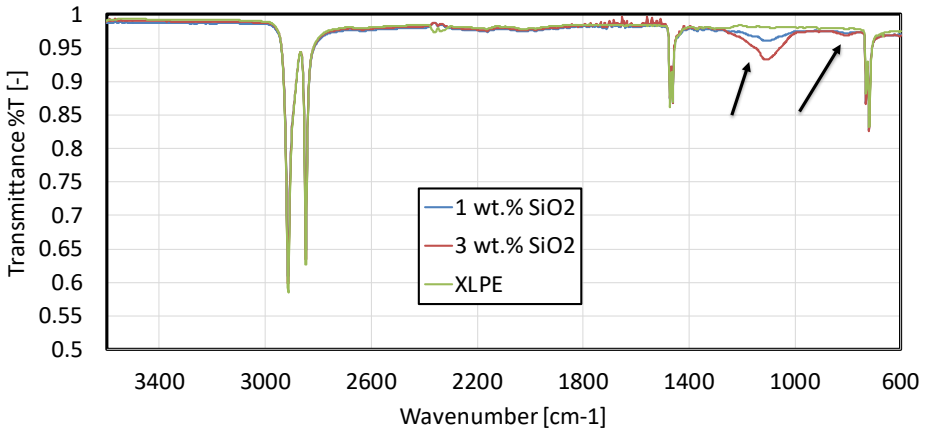

Fig. 36. FTIR spectra for XLPE nanodielectrics with different concentrations of SiO_2. Spectral changes associated with SiO_2 concentration are highlighted with arrows.

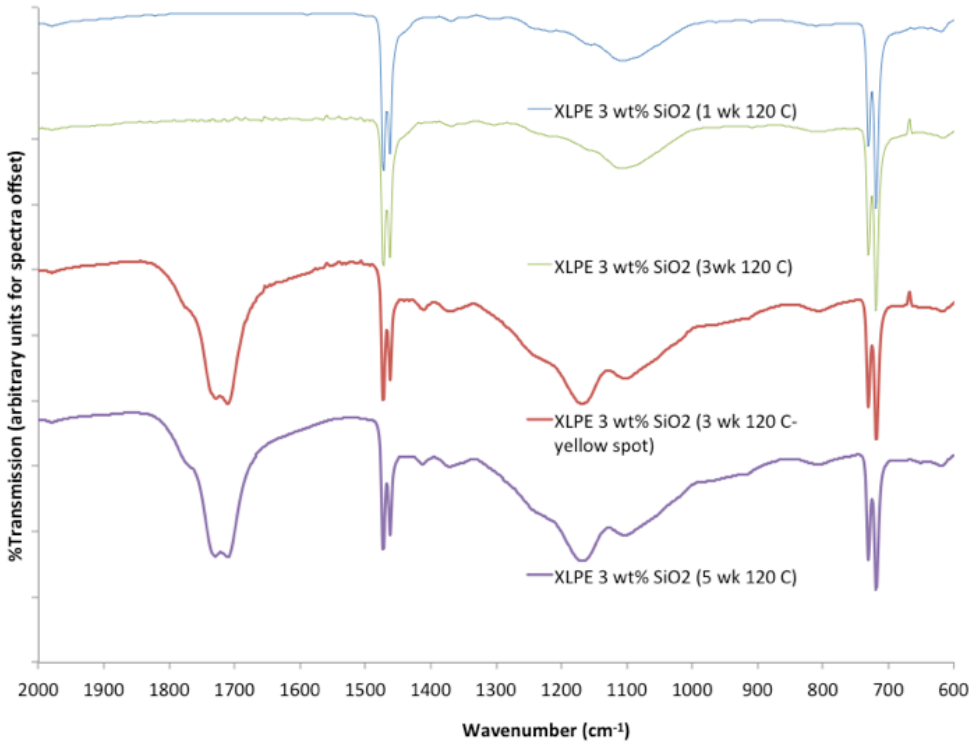

Fig. 37. ATR FTIR spectra for XLPE 3 wt % SiO_2 nanodielectrics aged thermally at 120°C.

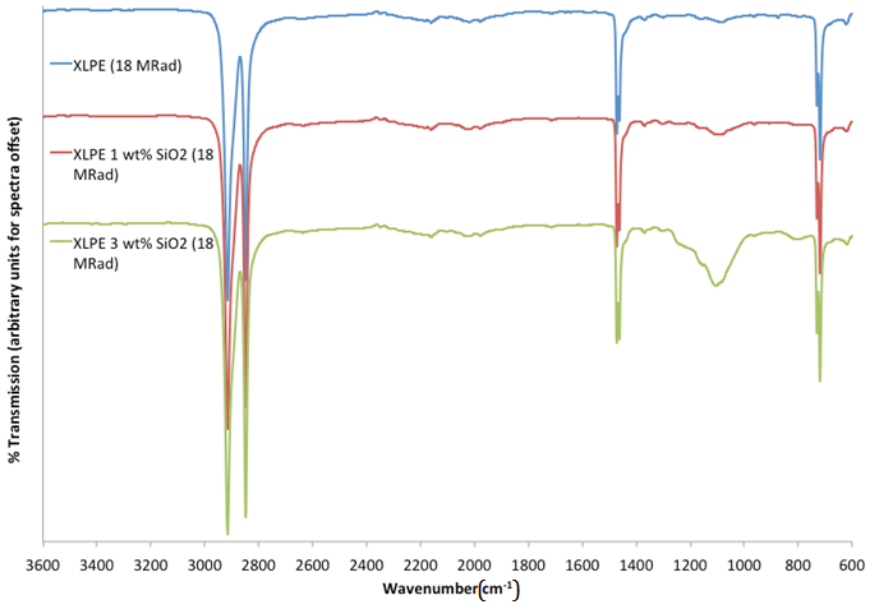

Fig. 38. ATR FTIR spectra for XLPE nanodielectrics with different concentrations of SiO_2 that have experienced gamma radiation for accumulated dose of 18 MRad in an argon atmosphere.

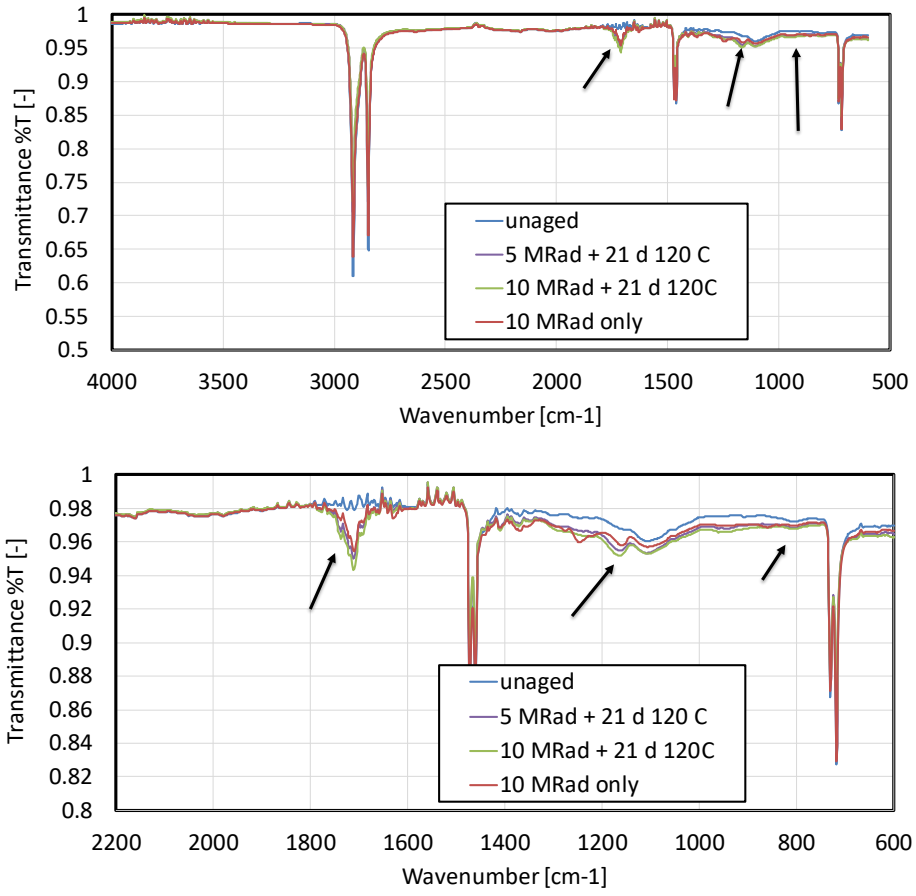

Fig. 39. FTIR spectra for XLPE nanodielectrics with 1 wt % SiO_2 at different environmental exposures *(top)* and the same FTIR spectra with emphasis on region below wavenumbers of 2000 cm^{-1} *(bottom)*.

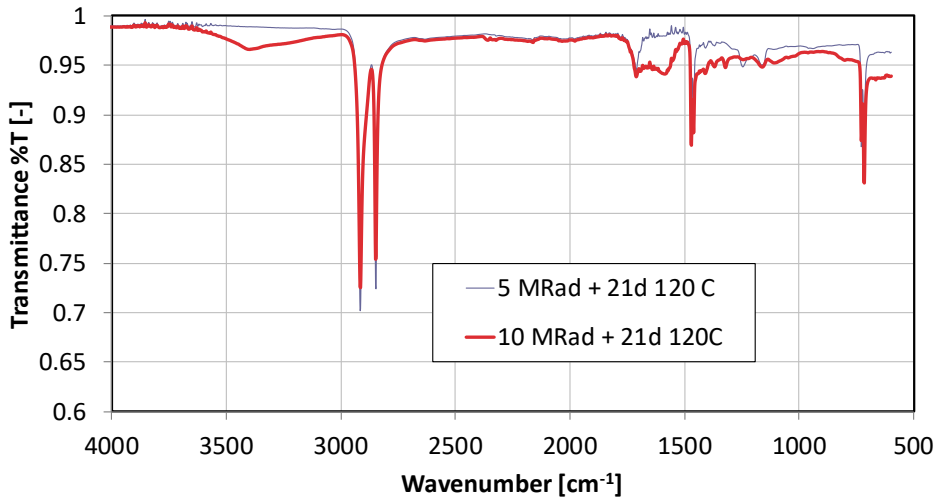

Fig. 40. FTIR spectra for XLPE nanodielectrics with 3 wt % MgO at different environmental exposures.

Electrical properties of XLPE nanodielectrics were affected by the percentage of nanoparticle before and after environmental exposures. Conductivity (Fig. 41) and permittivity as measured by dissipation factor (Fig. 42) show different functional dependencies with respect to weight percentage when compared to XLPVA films. Unlike XLPVA films, no composition showed decreased conductivity (increased resistivity) as the weight percentage was increased. However, the conductivity for the XLPE in all cases (including that shown in Fig. 38) was lower by three orders of magnitude compared to XLPVA. For the permittivity of the XLPE nanodielectrics, the frequency dependence and its magnitude were affected by the addition of SiO_2. This dependence can be viewed differently depending on the final application. If the dissipation factor needs to be as low as possible for high frequency insulations, reduction in dissipation factor can be achieved with a specific weight percentage of SiO_2. For frequency-dependent measurements such as frequency domain reflectometry which are often used to measure the condition of an insulation, a peak in dissipation factor could provide meaningful feedback on cable condition and temperature, especially if the temperature dependence of the permittivity shifts in the same manner as shown in Fig. 43 for an XLPE nanodielectric with 3 wt % SiO_2.

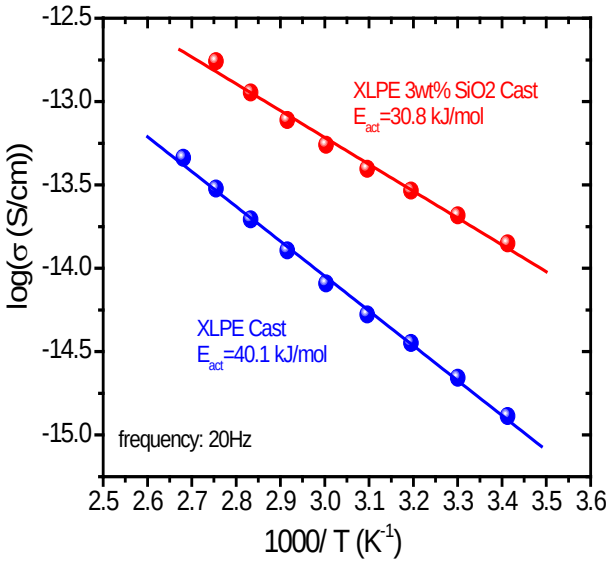

Fig. 41. Estimated conductivity of XLPE nanodielectric with respect to temperature (1000/T) and weight percentage of SiO_2.

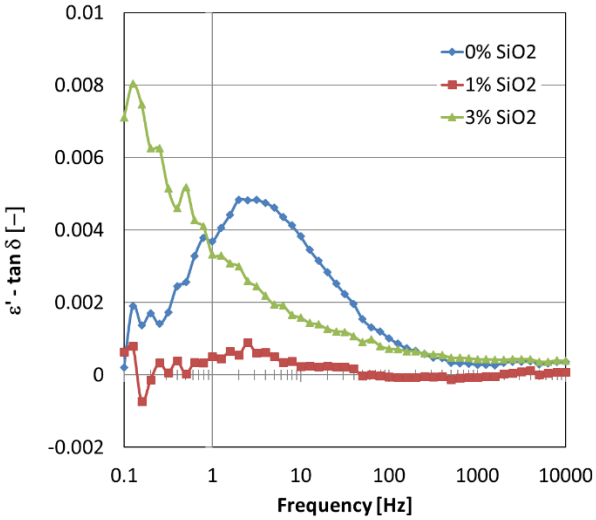

Fig. 42. Imaginary component of permittivity or dissipation factor, tan δ, for XLPE nanodielectric as a function of frequency and weight percentage of SiO_2.

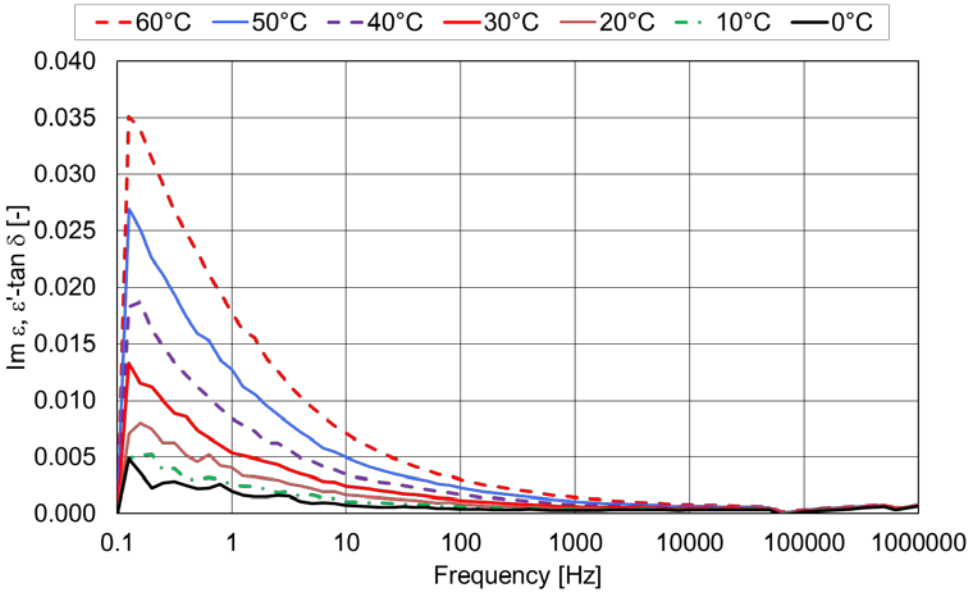

Fig. 43. Imaginary component of permittivity as a function of frequency and temperature for XLPE nanodielectric with 3 wt % SiO_2.

Dielectric breakdown strength of XLPE nanodielectrics was also affected by the weight percentage of nanoparticles before and after environmental exposure. Figure 44 shows a 10–15% increase in dielectric breakdown strength with 1 wt % SiO_2, but a drop by about 10% for 3 wt % SiO_2 when compared to the pure XLPE. When XLPE nanodielectrics were irradiated at the HFIR GIF in an inert environment, dielectric breakdown strength was observed to degrade, with the degradation increasing with weight percentage (Fig. 45). This is seen more clearly in Table 2 after a Weibull analysis was performed on the data from Fig. 45 as well other XLPE nanodielectrics exposed to the same conditions. The degradation was likely due to the ionization or the creation of defects within the XLPE when the amount of degradation is compared to little change in FTIR spectra observed in Fig. 38. For XLPE nanodielectrics after accelerated thermal aging at 120°C, degradation was also observed as indicated in Figs. 46 and 47 and the subsequent Weibull analysis in Table 3. The drop in dielectric breakdown strength for XLPE with and without SiO_2 coincided with the

increase in oxidation that was observed in FTIR spectra from Fig. 37. For XLPE MgO nanodielectrics, the drop in the dielectric breakdown strength was not as severe although the spread of dielectric breakdown strength in Fig. 47 suggests a significant amount of nonuniformity in the 5 week XLPE MgO nanodielectric. Nonuniformity was also observed in the limited amount of tensile testing performed, as shown in Fig. 48. While the results demonstrated possible improvement and optimization of XLPE nanocomposites, refinement is needed to ensure that the realized improvements are consistent.

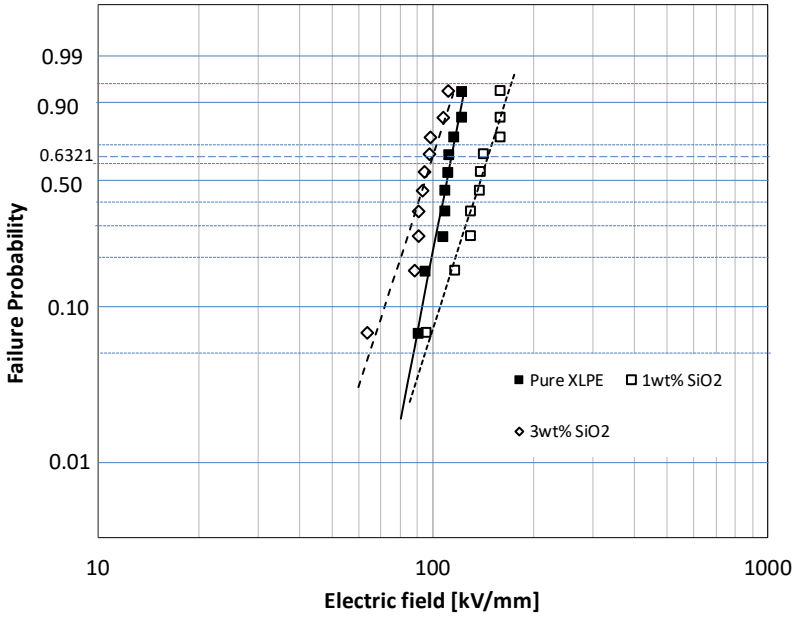

Fig. 44. Dielectric breakdown strength for XLPE nanodielectrics with different weight percentages of SiO_2.

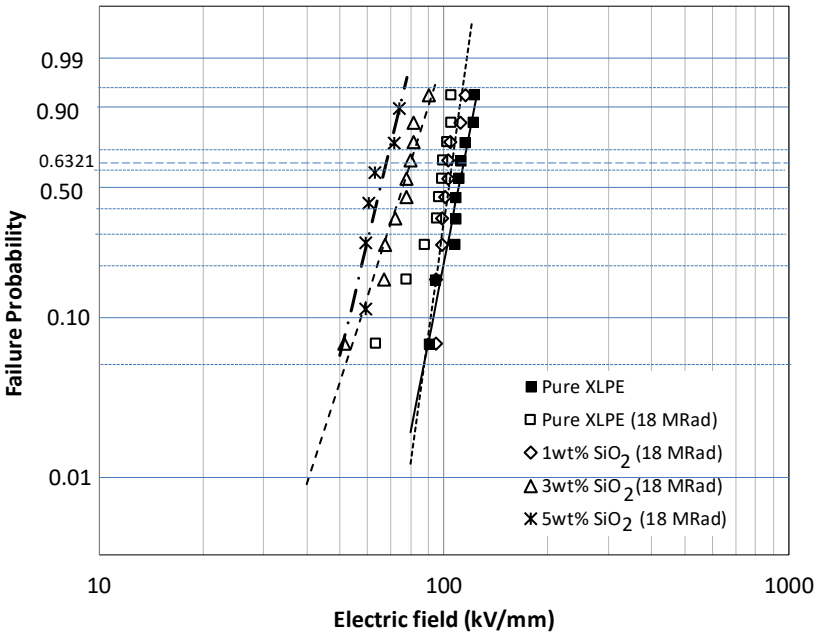

Fig. 45. Weibull distribution of dielectric breakdown strength for XLPE nanodielectrics with different concentrations of SiO_2 nanoparticles after an environmental exposure in argon atmosphere at 38°C and an accumulated gamma dose of 18 Mrad.

Table 2. Weibull scale and shape parameters for irradiated XLPE SiO_2 nanodielectrics after an environmental exposure in argon atmosphere at 38°C at different accumulated doses

Composition	Accumulated dose (MRad)	Weibull parameter α (kV/mm)	Weibull parameter β (-)
Pure	0	113.6	11.26
	10	97.6	15.42
	18	99.8	6.63
1 wt % SiO_2	0	146.0	6.35
	10	96.2	7.37
	18	105.6	15.90
3 wt % SiO_2	0	100.0	6.82
	10	101.9	10.37
	18	79.9	6.83
5 wt % SiO_2	0	n/a	n/a
	10	90.2	22.63
	18	68.0	9.20

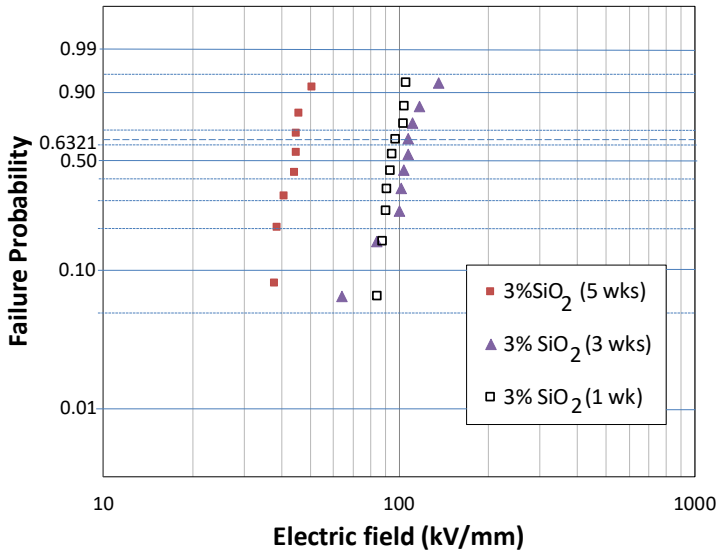

Fig. 46. Weibull distribution of dielectric breakdown strength for XLPE nanodielectrics with 3 wt % SiO_2 after different periods of accelerated thermal aging at 120°C.

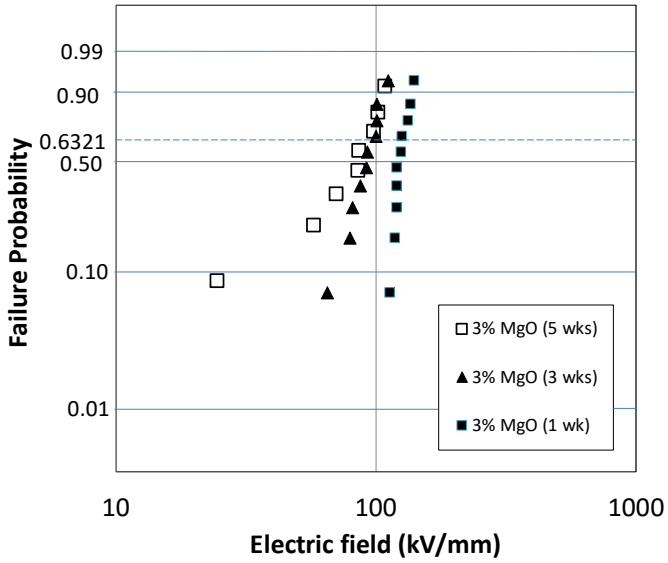

Fig. 47. Weibull distribution of dielectric breakdown strength for XLPE nanodielectrics with 3 wt % MgO after different periods of accelerated thermal aging at 120°C.

Table 3. Comparison of Weibull parameters and dissipation factor (tan δ) for XLPE nanodielectrics thermally aged at 120°C for different periods at a relative humidity between 45% and 55%

Composition	Time (weeks)	Weibull parameter α (kV/mm)	Weibull parameter β (-)	tan δ @ 1 kHz
Pure	1	126.4	7.82	0.0003
	3	92.6	12.86	0.0002
	5	55.0	5.64	0.0193
3 wt % SiO_2	1	98.5	14.40	0.0004
	3	112.2	5.26	0.0003
	5	45.6	10.76	0.0338
3 wt % MgO	1	129.3	15.71	0.0003
	3	97.0	7.08	0.0014
	5	92.3	20.10	0.0003

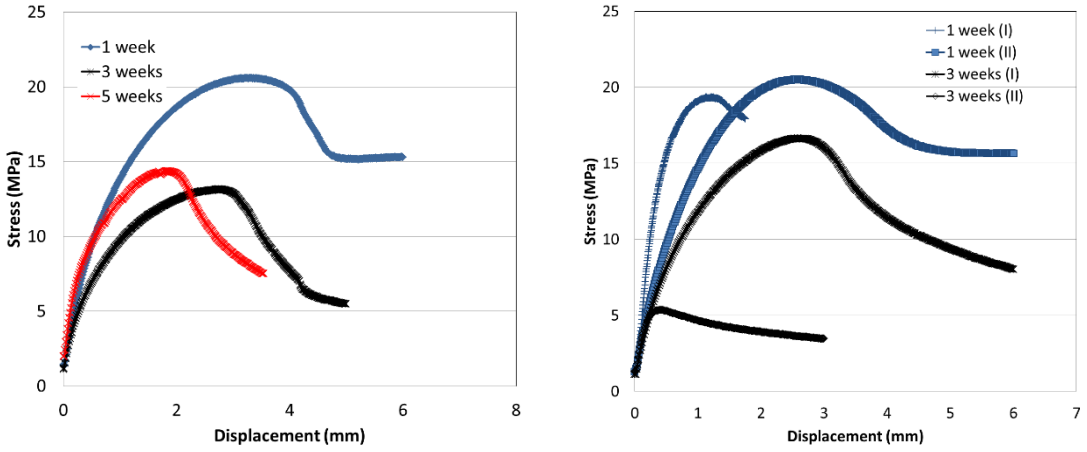

Fig. 48. Mechanical properties of XLPE without *(left)* and with *(right)* 3 wt % SiO_2 as a function of accelerated thermal aging at 120°C.

4.3 PI

Polyimide was the last base resin system investigated as part of this project. The amount of effort on PI nanodielectrics was limited with respect to PI processing optimization and environmental exposures due to feedback received at conferences and workshops from current nuclear power plant operators and cable aging management personnel. The use of PI has been limited in nuclear reactors due to findings of hydrolysis of PI when exposed to water during simulated LOCA exposures at high temperatures [33,34]. While the failure could have been attributed to the bonding of the adhesive to the PI, as PI is commonly used as a tape, additional resources beyond the existing scope of the project were needed to determine the feasibility of PI nanodielectrics with this additional failure mode. Based on the results presented in this section, there could be a benefit toward PI nanodielectrics in nuclear installations, but an evaluation of the baseline and accident environments is needed.

TEM images of PI films with different weight percentages of MgO are shown in Figs. 49 and 50. Agglomeration was clearly observed for the 5 wt % MgO case, while fiber-like features in Fig. 49 are assumed to be MgO. Further analysis via scanning electron microscopy indicated that the average particle size outside of those agglomerations observed was between 80 nm and 200 nm for both MgO and SiO_2. This particle size would support the sharp transition that was observed from the UV-Vis spectra in Fig. 51. As weight percentage increased, the transmittance dropped, as was seen in previous films when agglomeration and the number of particles within the polymer increased.

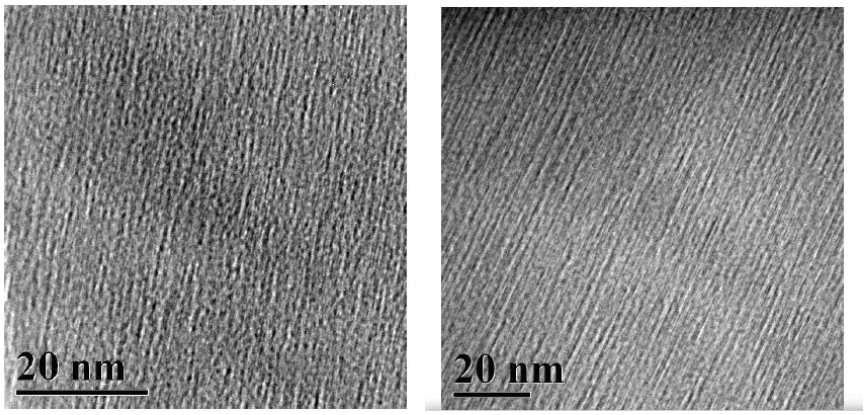

Fig. 49. TEM images of PI/MgO (3 wt %) nanodielectrics at two different sample locations.

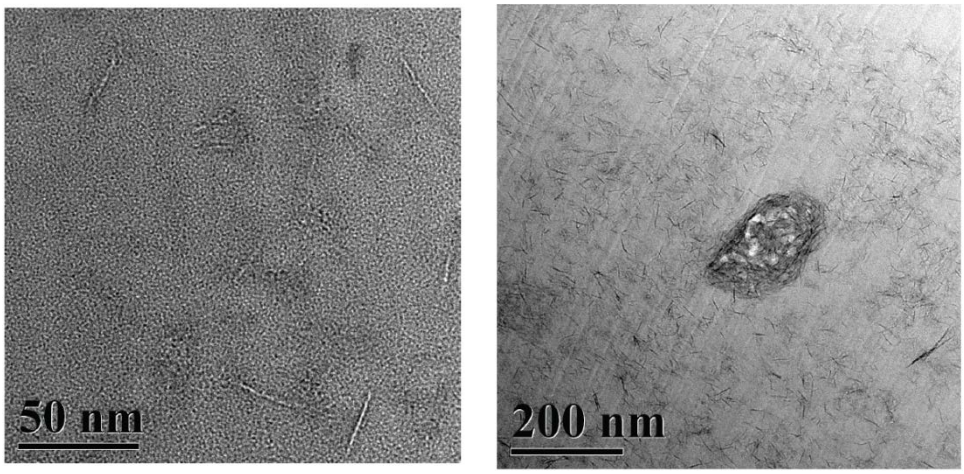

Fig. 50. TEM images of PI/MgO (5 wt %) nanodielectric at two different length scales.

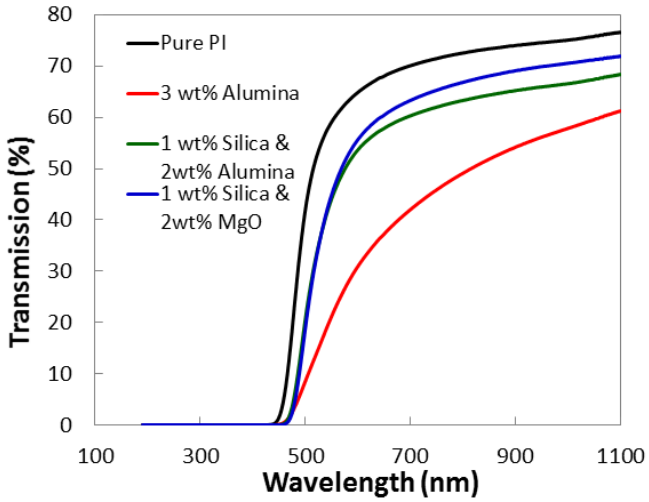

Fig. 51. UV-Vis spectra with respect to transmittance (T%) for PI nanodielectric films with different concentrations of nanoparticles.

The role of nanoparticle composition and imidization on the mechanical strength of PI nanodielectrics was examined using dynamic mechanical testing (DMA). Figures 52 and 53 show the functional dependence of the loss tangent, tan δ, which is the ratio of the storage modulus, E', to the loss modulus, E'', for pure PI base resin imidized at 200°C and PI with SiO_2 respectively. The peak near 300°C observed in Fig. 52 relates to the well-defined glass transition temperature, T_g, of the PI base resin. This peak, along with a secondary peak near 225°C, was also observed in PI nanodielectrics with different weight percentages of SiO_2. The secondary peak was attributed to incomplete imidization of the PI base resin.

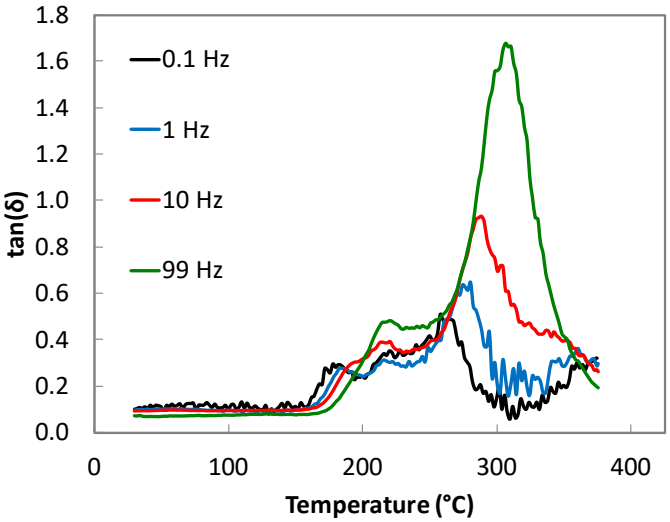

Fig. 52. Loss tangent (tan δ) of DMA characterization of PI base resin processed at 200°C as a function of frequency to illustrate the shift in glass transition temperature, which is found at maximum tan δ.

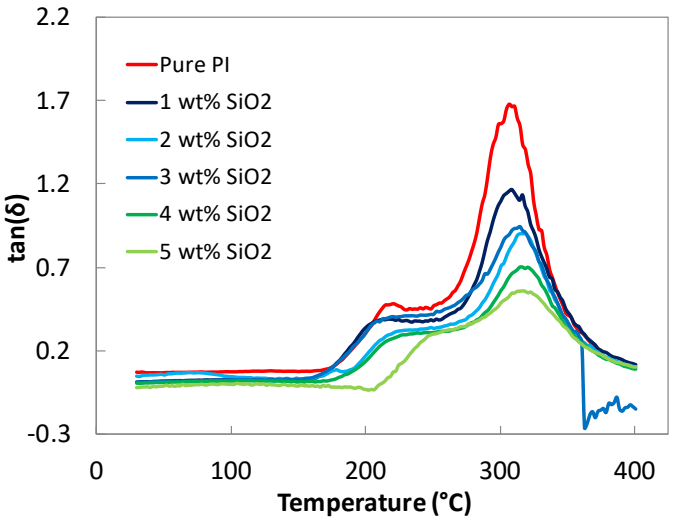

Fig. 53. Loss tangent (tan δ) of DMA characterization at 99 Hz of PI nanodielectrics as a function of SiO_2 weight percentage to illustrate the shift in glass transition temperature, which is found at maximum tan δ.

Table 4 shows the mechanical strength of the PI nanodielectrics expressed in terms of nanodielectric glass transition temperature, storage modulus, and activation energy, which were calculated from data similar to that shown in Figs. 52 and 53. In general, as the weight percentage increased, the mechanical strength increased, with the largest increases observed when MgO was added to PI. When select PI nanodielectrics were irradiated in an inert atmosphere up to 18 MRad, like the XLPE nanodielectrics, no significant decrease in sample performance was observed (Table 5). This lack of degradation was consistent with the lack of oxidation during this exposure.

Table 4. Summary of glass transition temperature, T_g, storage modulus, *E'*, and activation energy found from the frequency dependence of the glass transition temperature for PI nanodielectrics with different nanoparticle concentrations and compositions

Composition	T_g at 10 Hz (°C)	*E'* at 10 Hz and 300°C (Pa)	tan δ @ 1 kHz
Pure polyimide	288.4	1.62E+07	368±10
4 wt % SiO_2	308.4	6.70E+07	682±60
5 wt % SiO_2	310.3	9.43E+07	763±53
0.3 wt % MgO	306.3	4.88E+07	583±29
1 wt % MgO	318.3	1.26E+08	756±25
1 wt % Al_2O_3	310.3	3.82E+07	517±67
3 wt % Al_2O_3	317.3	1.41E+08	703±56
5 wt % Al_2O_3	324.3	1.49E+08	682±78
1 wt % MgO, 2 wt % SiO_2	333.4	2.85E+08	702±79
1.5 wt % MgO, 1.5 wt % SiO_2	322.3	1.64E+08	766±86
2 wt % MgO, 1 wt % SiO_2	341.4	3.53E+08	1372±101
2.5 wt % MgO, 0.5 wt % SiO_2	342.3	2.14E+08	1765±29
0.5 wt % Al_2O_3, 2.5 wt % SiO_2	316.3	1.88E+08	604±30
2 wt % Al_2O_3, 1 wt % SiO_2	314.3	1.02E+08	658±76

Table 5. Glass transition temperature, T_g, storage modulus, E', and activation energy found from the frequency dependence of T_g for PI nanodielectrics before and after irradiation up to 18 MRad at 38°C in an argon atmosphere

Composition	Before Irradiation			After Irradiation		
	T_g at 10 Hz (°C)	E' at 10 Hz and 300°C (Pa)	tan δ @ 1 kHz	T_g at 10 Hz (°C)	E' at 10 Hz and 300°C (Pa)	tan δ @ 1 kHz
1 wt % SiO_2	288.4	1.62E+07	368±10	299.2	5.35E+07	461±42
2 wt % SiO_2	308.4	6.70E+07	682±60	302.1	7.88E+07	569±41
3 wt % SiO_2	310.3	9.43E+07	763±53	306.2	7.82E+07	617±48
3 wt % MgO	306.3	4.88E+07	583±29	331.2	2.98E+08	2116±298

Finally, increasing the imidization temperature from 200°C to 300°C improved the mechanical properties of the PI base resin system (Fig. 54). This improvement was attributed to the disappearance of the loss tangent peak near 225°C for the PI base resin imidized at 200°C. The temperature 225°C is characteristic of the glass transition temperature of residual PAA, the unconverted precursor of PI. Its absence supports that the higher imidization temperature of 300°C resulted in the full conversion of PI. Additional work is needed to optimize PI nanodielectric processing and determine its sensitivity to the environment.

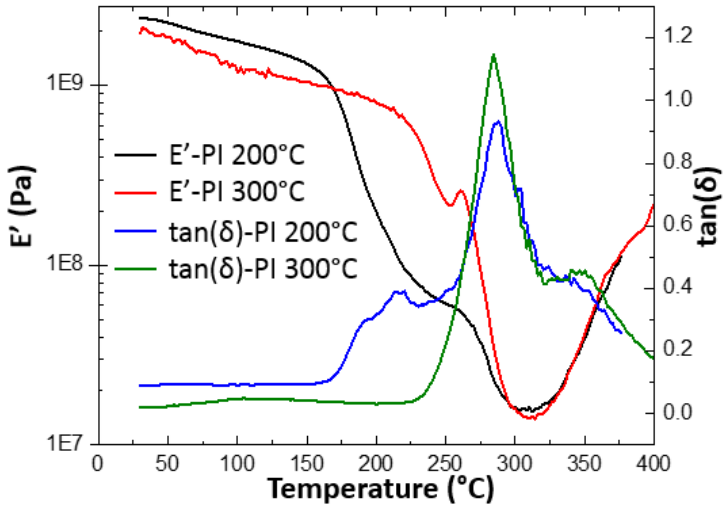

Fig. 54. DMA characterization of PI base resin with respect to storage modulus and loss tangent, tan(δ), as a function of imidization temperature.

Electrical properties (i.e., permittivity, dielectric breakdown strength, and voltage endurance) of the PI nanodielectrics were affected by nanoparticle composition and environmental exposure. Permittivity of PI nanodielectrics decreased by different percentages depending on the nanoparticle and weight percentage before and after accelerated thermal aging at 120°C (Fig. 55). This result suggests that permittivity could be used to track insulation degradation as part of a frequency domain reflectometry measurement for PI nanodielectric insulated conductors similar to the XLPE nanodielectrics. Dielectric breakdown strength of PI nanodielectrics also dropped depending on the concentration and environmental exposure (Figs. 56–58). Improvement in dielectric strength was observed for PI nanodielectrics with 1 wt % SiO_2, but this improvement did not carry through consistently after exposure of PI nanodielectrics to 18 MRad in an inert environment. Given the variation in performance observed, it is possible that agglomeration from one sample to the next at percentages close to 3 wt % could be the source of the inconsistency, but additional measurements and characterization are required.

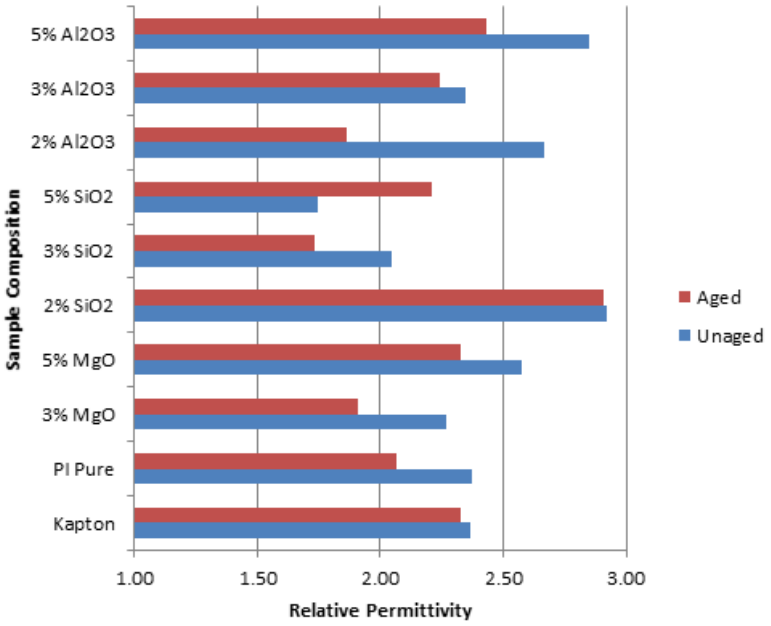

Fig. 55. Real permittivity for PI nanodielectrics with different nanoparticle concentrations before and after accelerated thermal aging for 4 weeks at 120°C in air.

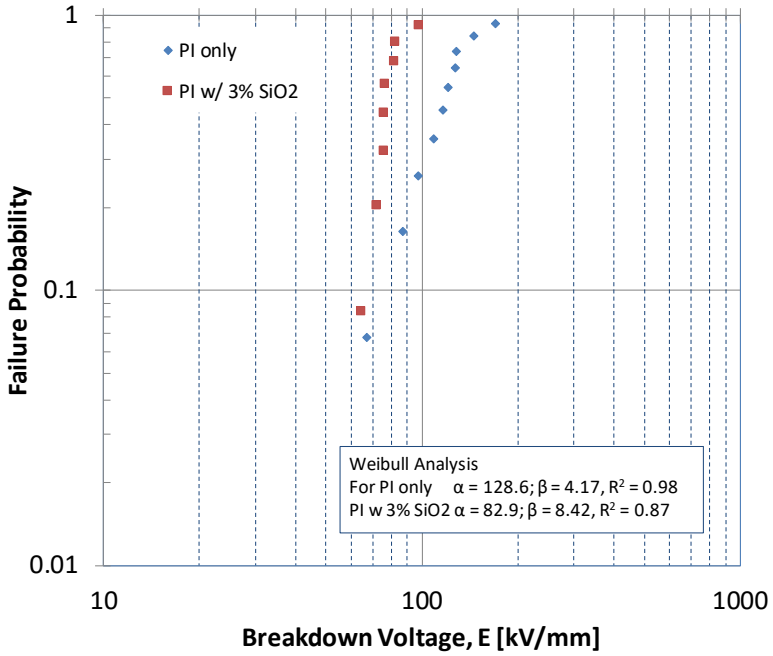

Fig. 56. Dielectric breakdown strength for PI nanodielectrics with and without 3 wt % SiO_2 nanoparticles.

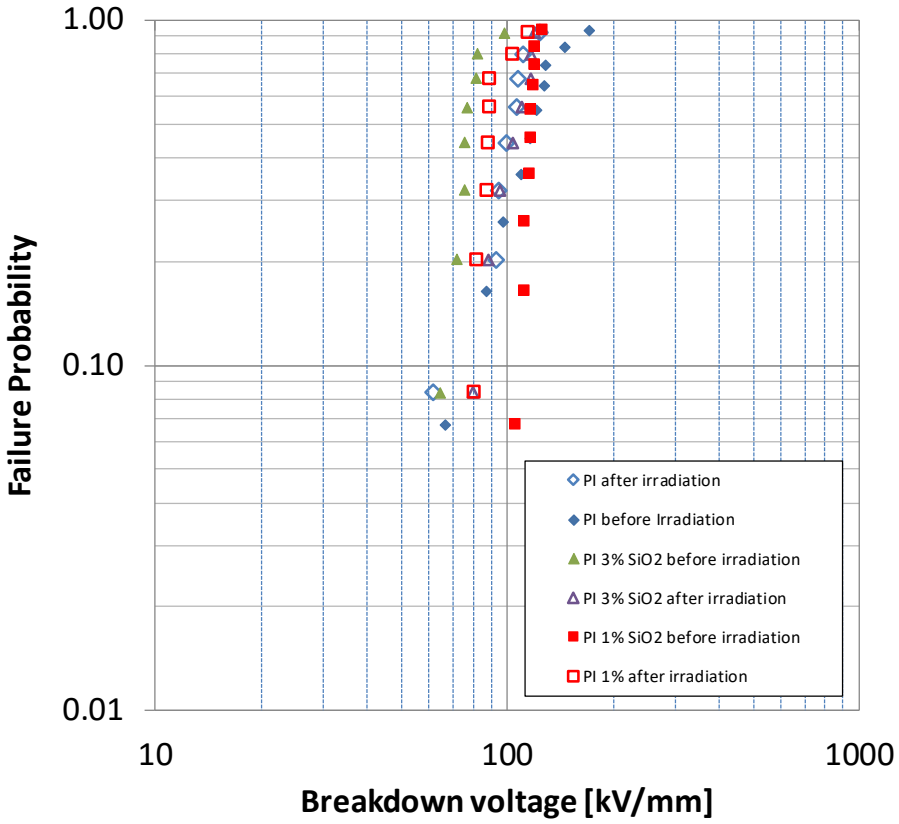

Fig. 57. Dielectric breakdown strength for PI nanodielectrics with different SiO_2 concentrations before and after irradiation to 18 MRad at 38°C in inert (argon) atmosphere.

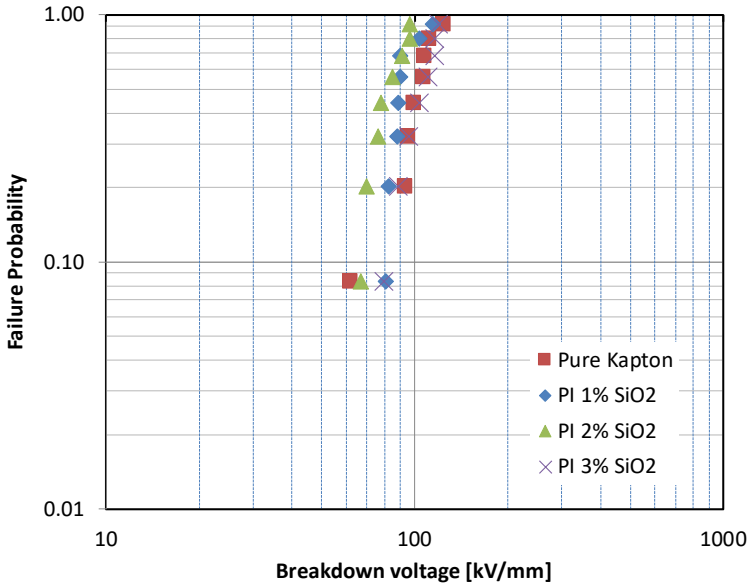

Fig. 58. Dielectric breakdown strength for PI nanodielectrics with different SiO_2 concentrations after irradiation to 18 MRad at 38°C in inert (argon) atmosphere.

Improvement was observed for voltage endurance measurements that were performed on PI nanodielectrics with 3 wt % and 5 wt % SiO_2 (Fig. 59), when compared to PI base resin. While the spread of the time to failure was broader for the PI nanodielectrics, the absence of the functional improvement

seen in previous work, as mentioned in Section 1 (Fig. 3), suggests that the improvement is not significant enough.

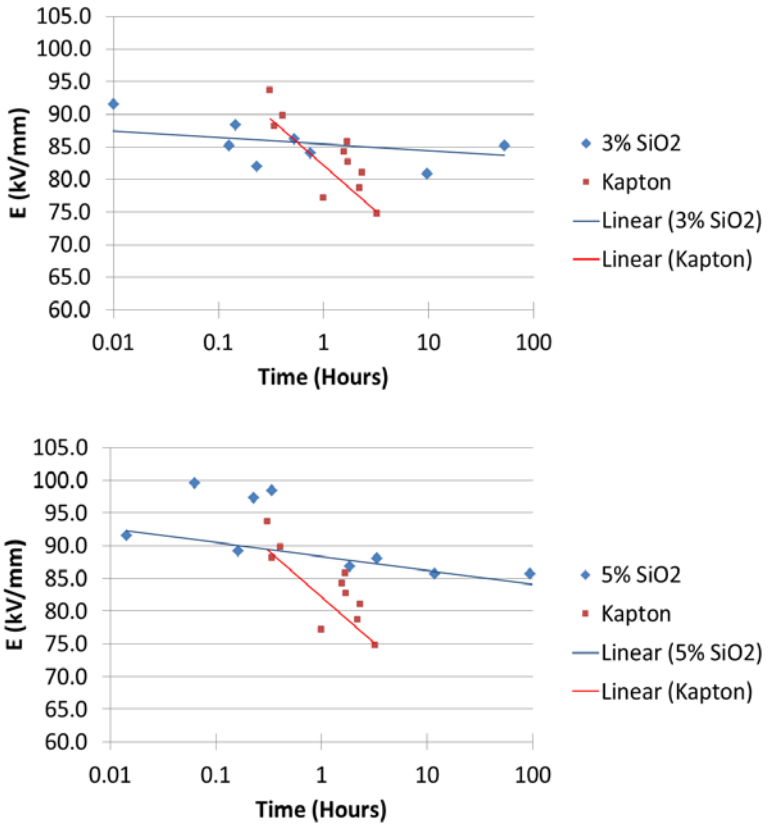

Fig. 59. Voltage endurance measurement for PI nanodielectrics without and with different SiO_2 concentrations [3 wt % SiO_2 *(top)* and 5 wt % SiO_2 *(bottom)*].

5. CONCLUSIONS AND RECOMMENDATIONS

The inclusion of nanoparticles in three separate material systems [cross-linked polyvinyl alcohol (PVA/XLPVA), cross-linked polyethylene (PE/XLPE), and polyimide (PI)] was successfully developed, and the chemical, electrical, and mechanical performance of each was analyzed as a function of environmental exposure and composition. Improvements were found in each material system; however, refinement of each processing pathway is needed, and the consequences of these refinements in the context of thermal, radiation, and moisture exposures should be evaluated before transferring knowledge to industry.

For PVA/XLPVA nanodielectrics:

- Uniform dispersion of SiO_2, TiO_2, and MgO was achieved with a measure of agglomeration for PVA nanodielectrics with TiO_2.
- A cross-linking process was developed for PVA to allow higher temperature processing with SiO_2 and MgO.
- Improvements in dielectric breakdown strength and conductivity were observed for certain configurations of PVA/XLPVA nanodielectrics between 1 and 5 wt %, depending on the specific nanoparticle composition.

For PE/XLPE nanodielectrics:

- FTIR indicated that SiO_2 and MgO bonded with the polymer chains of XLPE, although UV-Vis indicated that agglomeration could be occurring as the weight percentage increased.
- The change in the intensity of Si–O–Si and Si–O–C bonds as measured by FTIR in the XLPE nanodielectrics was affected by oxidation that occurred during thermal (up to 120°C) and radiation (up to 18 MRad) exposures. This oxidation depended on the weight percentage of the nanoparticle.
- The functional dependence of permittivity in XLPE nanodielectrics with respect to temperature, frequency, and weight percentage was observed. Combined with FTIR, frequency-based dielectric spectroscopy could be used as a condition monitor for the cables made from XLPE nanodielectric.
- Improvement in dielectric breakdown strength was observed, depending on the specific nanoparticle composition.

For PI nanodielectrics:

- Improvement in mechanical strength as measured via DMA was found for increasing weight percentages of nanoparticles and imidization temperature of the PI during its processing.
- Improvement in dielectric breakdown strength was also found, but variability of results suggests uniform dispersion issues.

While three different nanodielectrics were developed, further refinements are needed before each is ready for possible application to nuclear environments or other applications. For PVA nanodielectrics, the oxidation from thermal, radiation, and moisture needs to be understood. The advantage of PVA compared to the other nanodielectrics studied is that it is more mechanically flexible, which could be advantageous for nontraditional geometries and applications. For XLPE nanodielectrics, integration of the nanoparticles with respect to cross-linking and antioxidants remains an open question. Their usage in current XLPE production techniques could affect nanoparticle formation and the subsequent environmental degradation. Finally, for PI nanodielectrics, degradation with respect to moisture is the biggest hurdle for nuclear applications. The imidization temperature or processing modifications could affect the aqueous degradation of the PI, but this would require a more focused effort on this material system. The improvements in PI nanodielectrics realized in this project could be leveraged toward applications in low moisture, high radiation environments (e.g., accelerator magnets that use PI as part of the insulation structure). However, consideration of specific exposure conditions may require that as-yet-unstudied PI nanodielectric compositions be considered.

6. ACKNOWLEDGEMENTS

Research was sponsored and supported by the US Department of Energy Office of Nuclear Energy – Nuclear Energy Enabling Technologies – Reactor Materials program. This work was also supported by Oak Ridge Associated Universities (ORAU) through US Department of Energy–Science Undergraduate Laboratory Internships (SULI). This program allowed several undergraduate students from a diverse collection of institutions to contribute the technical results shown in this project. This group, as identified by their institution during the project, included Eric Greve (Hope College, Hope, MI), Jacob Johnson (Simpson College, Indianola, IA), Dustin Jones (University of Tennessee, Chattanooga), Obaid Khurram (North Central College, Naperville, IL), and Dylan Boucher (Allegheny College, Meadville, PA).

The authors would like to thank our ORNL collaborators and program management for providing access to different resources and invaluable expertise over the course of this project. These include Alvin Ellis, Joshua Perkins, Amit Naskar, Fue Xiong Tomonori Saito, Alexei Sokolov, Michelle Kidder, Ed Hagaman, Chris Bryan, Geoffery Deichert, Eric Mannerschmidt, Denise Lee, Caleb Robison, Jeremy Busby, and Isidor Sauers.

7. REFERENCES

[1] M.J. Jacobus, Aging, Condition Monitoring, and Loss-of-Coolant Accident (LOCA) Tests of Class 1E Electrical Cables, report NUREG/CR-5772, SAND91-1766/1, US Nuclear Regulatory Commission, 1992.

[2] T. Yamamoto, T. Minakawa, *The Final Report of the Project 'Assessment of Cable Aging for Nuclear Power Plants,'* report JNES-SS-0903, Japan Nuclear Energy Safety Organization, 2009.

[3] IEEE Standard for Qualification Class 1E Equipment for Nuclear Power Generating Stations, IEEE 323-1974, Institute of Electrical and Electronics Engineers, 1974.

[4] IEEE Standard for Qualification Class 1E Equipment for Nuclear Power Generating Stations, IEEE 323-2003, Institute of Electrical and Electronics Engineers, 2003.

[5] R. Bernstein, S. Burnay, C. Doutt, K. Gillen, R. Konnik, S. Ray, K. Simmons, G. Toman, G. von White, *Expanded Material Degradation Assessment, Volume 5: Aging of Cable and Cable Systems*, report NUREG/CR-7153 vol. 5, US Nuclear Regulatory Commission, 2014.

[6] H.M. Hashemian, W.B. Bean, "Sensors for next-generation nuclear plants: fiber-optic and wireless," *Nucl. Sci. Engr.* **169**(3), 262-278 (2011).

[7] B. Hay, K. Anhalt, L. Chapman, K. Boboridis, J. Hameury, S. Krenek, "High temperature thermophysical properties of advanced materials for nuclear design," pp. 71–76 in *Joint IMEKO TC11-TC19-TC20 Int. Symp. Metrological Infrastructure, Environmental and Energy Measurement and Int. Symp. of Energy Agencies of Mediterranean Countries*, report IMEKO-MI 2011, 2011.

[8] E. Tuncer, G. Polizos, I. Sauers, D.R. James, A.R. Ellis, K.L. More, *2009 Annual Report Conference on Electrical Insulation and Dielectric Phenomena (CEIDP 2009)*, IEEE, ISBN 9781424445578, pp. 527-530, 2009.

[9] Enis Tuncer et al., *Nanotechnology* **18**(2), 025703 (2007).

[10] Curbell Plastics website, http://www.curbellplastics.com.

[11] W.T. Shugg, Handbook of Electrical and Electronic Insulating Materials, IEEE Press: New York, 1995.

[12] Toshikatsu Tanaka et al., 2008 IEEE Conference on Electrical Insulation and Dielectric Phenomena - (CEIDP 2008), IEEE, ISBN 9781424425495, pp. 13-16, 2008.

[13] L.K. Mansur, K. Farrell, *J. Nucl. Mater*. **244**, 212-218 (1997).

[14] J.S. Forsythe, D.J.T. Hill, *Prog. Polym. Sci*. **25**, 101-136 (2000).

[15] J. Davenas et al., *Nucl. Instr. Methods Phys. Res*. **B191**, 653-661 (2002).

[16] S. Wang, J.M. Legare, *J. Fluorine Chem.* **122**, 113-119 (2003).

[17] R.H. Partridge, *J. Chem. Phys*. **52**(5), 2501-2510 (1970).

[18] D.J.Y.S. Pagé, H.W. Bonin, V.T. Bui, P.J. Bates, *J. Appl. Polymer Sci*. **86**, 2713-2719 (2002).

[19] J.S. Forsythe, D.J.T. Hill, A. L. Logothetis, T. Seguchi, A.K. Whittaker, *Rad. Phys. Chem.* **53**, 611-621 (1998).

[20] W.W. Parkinson, O. Sisman, *Nucl. Eng. Design* **17**, 247-280 (1971).

[21] K.T. Gillen, R.L. Clough, *Radiat. Phys. Chem*. **18**(3-4), 679-687 (1981).

[22] R. Venckatesh, K. Balachandaran, R. Sivaraj, "Synthesis and characterization of nano TiO_2-SiO_2: PVA composite – a novel route," *Int. Nano Lett.* **2**(15), 1-5 (2012).

[23] L. Liu, C. Zhao, F. Yang, "TiO_2 and polyvinyl alcohol (PVA) coated polyester fiber for bioreactor for waterwater treatment," *Water Res.* **46**, 969-1978 (2012).

[24] K. Chrissafis, K. Parakevopoulos, G.Z. Papageorgiou, D.N. Bikiaris, "Thermal and dynamic mechanical behavior of bionanocomposites: fumed silica nanoparticles dispersed in poly(vinyl pyrrolidone, chitosan, and poly(vinyl alcohol)," *J. Appl. Poly. Sci.* **110**, 1739-1749 (2008).

[25] L. Reijnders, "The release of TiO_2 and SiO_2 nanoparticles from nanocomposites," *Poly. Deg. Stab.* **94**, 873-876 (2009).

[26] M. Roy, J.K. Nelson, R.K. MacCrone, L.S. Schafer, "Candidate mechanisms controlling the electrical characteristics of silica/XLPE nanodielectrics," *J. Mater. Sci*. **42**, 3789-3799 (2007).

[27] Z. Ma, X. Huang, P. Jiang, G. Wang, "Effect of silane-grafting of Water tree resistance of XLPE cable insulation," *J. Appl. Poly. Sci*. **115**, 3168-3176 (2010).

[28] K. Sirsinha, M. Boonkongkaew, S. Kositchaiyong, "The effect of silane carriers on silane grafting of high-density polyethylene and properties of crosslinked products," *Poly. Test.* **29**, 958-965 (2010).

[29] H. Azizi, J. Barzin, J. Morshedian, "Silane crosslinking of polyethylene: the effects of EVA, ATH, and Sb_2O_3 on properties of the production in continuous grafting of LDPE," *Poly. Lett.* **1**, 378-384 (2007).

[30] H.-C. Kuan, J.-F. Kuan, C.-C. M. Ma, J.-M. Huang, "Thermal and mechanical properties of silane-grafted water crosslinked polyethylene," *J. Appl. Poly. Sci.* **96**, 2383-2391 (2005).

[31] M.B. Radočić, Z.V. Šaponjić, M.T. Marinović-Cincović, S.P. Ahrenkiel, N.M. Bibić, J.M. Nedeljković, "The influence of shaped TiO_2 nanofillers on the thermal properties of poly(vinyl alcohol)," *J. Serb. Chem. Soc.* **77**, 699-714 (2012).

[32] IEEE Guide for Statistical Analysis of Electrical Insulation Breakdown Data, IEEE 930-2004, Institute of Electrical and Electronics Engineers, 2004.

[33] G.J. Toman, P.J. Lindsay, *Review of Polyimide Insulated Wire in Nuclear Power Plants*, Electrical Power Research Institute, report NP-7189 (1991).

[34] F.J. Campbell, "Temperature Dependence of Hydrolysis of Polyimide Wire Insulation," *IEEE on Elec. Ins.*, **EI-20**, 111-116 (1985).